their quantities are shown in figure 2. In lower collagen content (1#), the plate-like nano-CHA (figure 2(*A*)) was changed into needle-like CHA when the carbonate was slightly increased, as illustrated in figures 2(*B*) and (*C*). When the carbonated content reached 6.9% of 13#, the length of the needle-like nanocrystals decreased significantly (figure 2(*C*)). Moreover, the nCHA crystals assembled along the longitude axes to a certain degree. This is the first time where the effect of carbonate on nCHAC self-assembly is seen. When the carbonated percentage is too high, the crystal became spherical, which is shown in figure 2(*D*). When the content of collagen increased to approximately 16% (2#), the morphologies of the composites were drastically changed. The crystalline sizes decreased tremendously, and this was confirmed from XRD results. Another observation was that the assembled units could be seen in composites with higher collagen content such as those in 21# and 22# (figures 2(*G*) and (*H*), black circles referred). In figure 2(*I*), the deficient crystals are prominently defined. As a result, the assembled units were not clearly observable in 23# samples. From the TGA results, the morphologies of the crystals (22# and 23#) were contrasting despite the similar final carbonate content present in these materials. It was only after the content of collagen has reached a certain level that the self-assembly of collagen and nCHA could be achieved. There could be some relations with regard to the assembled unit in 2# nCHAC composite and the short needle-like nCHA in 13# sample. Generally, nCHA grows along the collagen fibril, and when sufficient collagen is self-assembled into fibril bundles, the mineralized fibril bundles subsequently appear as an assembled unit. Likewise, for 1#, when the carbonated content is exceedingly high, the formed 24# composite became small spheres of nanocrystals, and their sizes were smaller than those of 14#. In summary, the morphological results may provide us with the perspicuity for designing biomimetic apatites/collagen composites with optimized performances according to the various clinical applications.

Conclusion

The nano-carbonated hydroxyapatite/collagen (nCHAC) composite was prepared via a biomimetic self-assembly method by different collagen and carbonated incorporation. With higher collagen content, lower crystal size of nCHAC was obtained. With higher carbonate content, the plate-like crystals of the composites gradually changed into needle-like crystals, followed by short needle-like structures, eventually becoming spherical particles. The microstructure of this composite with a mineralized collagen fiber bundle similar to that of natural bone was only seen when a certain combination of carbonate and collagen components was present.

Acknowledgments

This work was supported in part by the JSPS Program in Japan, and NUS LKY PDF fellowship in Singapore.

References

[1] Kikuchi M, Itoh S, Ichinose S, Shinomiya K and Tanaka J 2001 Self-organization mechanism in a bone-like hydroxyapatite/collagen nanocomposite synthesized in vitro and its biological reaction in vivo *Biomaterials* **22** 1705–11

[2] Zhang W, Liao S S and Cui F Z 2003 Hierarchical self-assembly of nano-fibrils in mineralized collagen *Chem. Mater.* **15** 3221–26

[3] Liao S S, Cui F Z, Zhang W and Feng Q L 2004 Hierarchically biomimetic bone scaffold materials: nano-HA/collagen/PLA composite *J. Biomed. Mater. Res.* B **69** 158–65

[4] Landi E, Celotti G, Logroscino G and Tampieri A 2003 Carbonated hydroxyapatite as bone substitute *J. Eur. Ceram. Soc.* **23** 2931–37

[5] Tadic D and Epple M 2004 A through physicochemical characterization of 14 calcium phosphate-based bone substitution materials in comparison to natural bone *Biomaterials* **25** 987–94

[6] Suchanek W J, Shuk P, Byrappa K, Riman R E, TenHuisen K S and Janas V F 2002 Mechanochemical-hydrothermal synthesis of carbonated apatite powders at room temperature *Biomaterials* **23** 699–710

[7] Tadic D, Peters F and Epple M 2002 Continuous synthesis of amorphous carbonated apatite *Biomaterials* **23** 2553–9

[8] Leventouri Th 2006 Synthetic and biological hydroxyapatites: crystal structure questions *Biomaterials* **27** 3339–42

[9] Du C, Cui F Z, Zhang W, Feng Q L, Zhu X D and de Groot K 2000 Formation of calcium phosphate/collagen composites through mineralization of collagen matrix *J. Biomed. Mater. Res.* **50** 518–27

[10] Du C, Cui F Z, Zhu X D and de Groot K 1999 Three-dimensional nano-HAp/collagen matrix loading with osteogenic cells in organ culture *J. Biomed. Mater. Res.* **44** 407–15

[11] Liao S S, Cui F Z and Zhu Y 2004 Osteoblasts adherence and migration through three-dimensional porous mineralized collagen based composite: nHAC/PLA *J. Bioact. Comp. Polym.* **19** 117–30

[12] Liao S S, Guan K, Cui F Z, Shi S S and Sun T S 2003 Lumbar spinal fusion with a mineralized collagen matrix and rhBMP-2 in a rabbit model *Spine* **28** 1954–60

[13] Liao S, Watari F, Uo M, Ohkawa S, Tamura K, Wang W and Cui F Z 2005 The preparation and characteristics of a carbonated hydroxyapatite/collagen composite at the room temperature *J. Biomed. Mater. Res.* B **74** 817–21

[14] Liao S, Wang W, Uo M, Ohkawa S, Aksaka T, Tamura K, Cui F Z and Watari F 2005 A three-layered nano-carbonated hydroxyapatite/collagen/PLGA composite membrane for guided tissue regeneration *Biomaterials* **26** 7564–71

[15] MDI JADE6 software, XRD pattern processing, Materials Data, Inc, 2003

[16] Klug H P and Alexander L E 1974 *X-ray Diffraction Procedures for Polycrystalline and Amorphous Materials* (New York: Wiley)

[17] Peters F, Schwarz K and Epple M 2000 The structure of bone studied with synthrotron x-ray diffraction, x-ray absorption spectroscopy and thermal analysis *Thermochim. Acta* **361** 131–8

[18] LeGeros R Z 1991 *Calcium Phosphates in Oral Biology and Medicine* (Basel, Switzerland: Karger AG)

[19] Landis W J, Song M J and Leith A 1993 Mineral and organic matrix interaction in normally calcifying tendon visualized in three dimensions by high-voltage electron microscopic tomography and graphic image reconstruction *J. Struct. Biol.* **110** 39–54

[20] Lowenstam H A and Weiner S 1989 *On Biomineralization* (New York: Oxford University Press) pp 35–40

DENTAL MATERIALS 23 (2007) 1120–1128

available at www.sciencedirect.com

ScienceDirect

journal homepage: www.intl.elsevierhealth.com/journals/dema

The degradation of the three layered nano-carbonated hydroxyapatite/collagen/PLGA composite membrane in vitro

Susan Liao[a,*], *Fumio Watari*[a], *Yuhe Zhu*[a], *Motohiro Uo*[a], *Tsukasa Akasaka*[a], *Wei Wang*[a], *Guofu Xu*[b], *Fuzhai Cui*[c]

[a] *Graduate School of Dental Medicine, Hokkaido University, Sapporo 060-8586, Japan*
[b] *Department of Materials Science and Engineering, Central South University, Changsha 410083, PR China*
[c] *Department of Materials Science and Engineering, Tsinghua University, Beijing 100084, PR China*

ARTICLE INFO

Article history:
Received 19 August 2005
Received in revised form
10 March 2006
Accepted 22 June 2006

Keywords:
Biodegradation
Nano-carbonated hydroxyapatite
Guided tissue regeneration

ABSTRACT

Objective. The purpose of this paper was to investigate the in vitro biodegradation of a guided tissue regeneration composite membrane, nano-carbonated hydroxyapatite/collagen/poly(lactic-co-glycolic acid) (nCHAC/PLGA). Especially for periodontal therapy, the functional graded material (FGM) nCHAC/PLGA membrane was prepared that consisted of three layers with 8 wt% nCHAC + PLGA/4 wt% nCHAC + PLGA/PLGA, where one face of the membrane is porous, thereby allowing cell growth thereon and the opposite face of the membrane smooth, thereby inhibiting cell adhesion.

Methods. For evaluation, in vitro degradation specimens of nCHAC/PLGA were immersed into artificial saliva solution at 37 °C for 1, 2, 4, 8 and 12 weeks to detect the weight loss over the period, and set pure PLGA membrane as control to compare the degraded behaviors. pH value and calcium concentration of the residual solution were measured, and morphology change was investigated by scanning electron microscopy (SEM).

Results. During the experimental period in vitro, the whole shape of the membrane could be kept for 4 weeks, after that it became powder at between 8 and 12 weeks. The results demonstrated that weight loss increased continuously with a reduction in mass of 23.1% after 4 weeks and 88% after 12 week for the nCHAC/PLGA three FGM layers composite membrane. The calcium concentration in the residual solution showed a significant increase after 4 weeks, which referred to the nano-carbonated hydroxyapatite degradation. Moreover, the pH value in the solution of the nCHAC/PLGA membrane was a little higher than that of the pure PLGA membrane, which demonstrated the possible neutralization effect from nCHAC composite for the acid outcome of PLGA in the solution. The pore structure of 8 wt% nCHAC + PLGA was enlarged on the porous surface, while the nonporous surface of pure PLGA also showed a small porous structure after increased time.

Significance. Degradation of the composite membrane is appropriate for practical periodontal repair. Moreover, the new mineral formation on the surface of the composite membrane referred to the possible positive effect in vivo for new bone tissue regeneration.

* *Corresponding author at:* Department of Oral Health Science, Graduate School of Dental Medicine, Hokkaido University, Kita Ku Kita13 Nishi 7, Sapporo 060-8586, Japan. Tel.: +81 11 706 4252; fax: +81 11 706 4251.
E-mail addresses: liaosusan@tsinghua.org.cn, liao@den.hokudai.ac.jp (S. Liao).

0109-5641/$ – see front matter © 2006 Academy of Dental Materials. Published by Elsevier Ltd. All rights reserved.
doi:10.1016/j.dental.2006.06.045

1. Introduction

Thin, reabsorbed polymer membranes have recently been developed and tested in GTR applications, which comprise either polylactic acid (PLA) blended with a citric acid ester or a copolymer made of glycolide and lactide polymers (PLGA). Polyesters can easily be processed into the desired configuration, and physical, chemical, mechanical, and degradation properties can be engineered to fit a particular need [1]. They have low immunogenicity and toxicity, and their excellent biocompatibility has also been demonstrated in many biological systems [2–4]. They have found widespread use in clinical medicine for bone fixation, surgical suture, as a scaffold for tissue engineering, and for controlled drug release [5–8]. Degradation properties are of crucial importance in biomaterial selection and design. The rate of degradation may affect a range of processes, such as cell growth, tissue regeneration, drug release, and host response. These polymers degrade directly to acid during the resorption process. However, medical devices made from this type of reabsorbed polymer membrane have been associated with an inflammatory response, which may be caused by the accumulation of the acid of the degraded product. Most of the research has focused on their degradation properties, but only a few studies on the morphological changes of porous materials [2–4]. Lu et al. even found the heterogeneous bulk degradation of thin PLGA film in vitro in PBS. The differential morphology of the porous inner layer and nonporous surface layer was due to autocatalysis in the specimen center [9]. For porous membranes of PLA and PLGA, the porosity and pore sizes were mainly influenced by the molecular weight of the polymers and the concentration of polymer solutions: the composition ratio of the lactide and glycolide in the copolymer did not significantly affect the porous structure [10].

In a previous work nano-HA/Collagen (nHAC) based composite through the self-assembled co-precipitation method was prepared similar to that of natural bone and to demonstrate the high cell affinity and bioactivity in vivo [11–15]. In order to increase resorption in vivo, nano-carbonated hydroxyapatite/collagen (nCHAC) composite was prepared at room temperature [16]. This composite shows the same inorganic phase of natural bone of nano-sized level and low degree of crystallinity, and contains 2.8–14.7 wt% of carbonated content [16]. Many experiments show the high solubility of carbonated apatite in vitro and in vivo [17,18]. The HA phase present in natural bone, dentin and enamel, respectively, contains approximately 7.4, 5.6 and 3.5 wt% of carbonate [19]. CHA materials have excellent biocompatibility and properties, which can be favorably compared with those of hard tissue. As we know, higher carbonated minerals are in accord with higher osteoconductivity and earlier bioresorption. In the current study the authors selected nCHAC as the bioactive component, PLGA as the barrier to prepare one novel three-layered membrane comprising a pliable not brittle, substantially cell-impermeable polymeric layer, a first cell-permeable outer layer superimposed on a first surface of the outer layer, and a second cell-permeable outer layer superimposed on a second surface of the inner layer, opposite the first face. The three-layered graded membrane, with one face of 8% nano-carbonated hydroxyapatite/collagen/poly(lactic-co-glycolic acid) (nCHAC/PLGA) porous membrane, the opposite face of pure PLGA nonporous membrane, the middle layer of 4% nCHAC/PLGA as the transition was prepared by a layer-by-layer casting method. Then the three layers were well combined with one another with flexibility and enough high mechanical strength as a membrane, because the three layers all contained PLGA polymer that can be easily used for practical medical application. This high biocompatibility and osteoconductivity of this biodegraded composite membrane was enhanced by the addition of nCHAC, for the same component and nano-level crystal size with natural bone tissue. The nCHAC material facilitates reliable bone regeneration by inducing undifferentiated cells in the graft recipient site to become osteoblasts and form new bone (i.e., stimulating cellular transformation). The composite also supplied a ready source of calcium for rapid mineralization. The barrier material is easy to use during surgery and is completely biodegradable, eliminating the need for second surgery to remove the barrier material. This new mineralized collagen/PLGA membrane is considered to have many medical applications because of its flexibility, strong mechanical strength, easy manipulation character, excellent biocompatibility and controllable bioresorption. Such medical applications for repairing periodontal defects, membranes for covering bone defect surgery and for bone substitutes, skin wound repair and healing, skin sealing, and as a carrier for antibiotic, bone growth factors, skin growth factors, and so forth.

Therefore, in this study, the authors concentrated on the degraded ratio and the morphological changes in two different surfaces of three-layered nCHAC/PLGA composite membrane during degradation in vitro; one is the PLGA nonporous face and the other is the nCHAC/PLGA porous composite face. By comparing the different degradation behaviors of this composite membrane to pure PLGA membrane with only the same nonporous surfaces as control, the authors investigated the effect of nCHAC addition during the 12 weeks degradation period. For this experiment, artificial saliva solution was selected as the degradation media in vitro, not simulated body fluid (SBF). There are two reasons: one is the direct application guidance in the oral medical field, the other is the relatively simple component in the solution, which is helpful for investigating the biodegradation mechanism. The artificial saliva and SBF are both phosphate balanced solutions of about pH 7.4. Moreover, there is much research work on the apatite formation on the several substrates in modified SBF, such as Ti, Ti alloy, polymer, sintered hydroxyapatite, etc. [20–23]. Little attention has been paid to the reaction of biomaterials in artificial saliva solution, even in materials used in dentistry. Then we can compare the different reactions of the biomimetic material in SMF and artificial saliva solution, which may help us to fully understand the reactions in vivo.

2. Materials and methods

2.1. *nCHAC/PLGA FGM composite membrane fabrication*

Nano-carbonated hydroxyapatite/collagen composite (nCHAC) was prepared by the biomimetic method, which

has been reported previously [16]. Briefly, Type 1 atelocollagen gel (2 wt%, Koken Company, Japan) was added to 0.5 M acetic acid. Then solutions of $CaCl_2$ and H_3PO_4 (Ca/P = 1.66) were gradually added separately through respective tube pumps and after stirring for 1 h, the solution of Na_2CO_3 (mol ratio of $CO_3^{2-}/PO_4^{3-} = 3$), was gradually added. All chemical reagents were of especially pure quality for research from Kanto Chemical Co. Inc., Tokyo, Japan. Then it was stirred, titrated with sodium hydroxide to pH 9 at room temperature. After aging the solution for more than 2 h, the nCHAC material was harvested by centrifuging and freeze-drying. The second step, the nCHAC/PLGA composite membrane with three graded layers was prepared by the following method, which has previously been reported [24]. Three 5 g units 75/25 PLGA (0.72 dl/g inherent viscosity, Absorbable Polymers International, USA) were dissolved successively by stirring into 20 ml chloroform. The first solution was for Layer 1. The second one was added to 0.2 g nCHAC prepared above, and ultrasonically mixed for Layer 2. The third one was added to 0.4 g nCHAC prepared above, and ultrasonically mixed for Layer 3. 1 ml of the first solution was poured into a glass Petri dish, allowed to sit for 30 min at room temperature, which was sufficient to form into Layer 1. Then 1 ml of the second solution was poured into Layer 1 wherein the surfaces bounded by Layer 1 formed Layer 2. 30 min later, 1 ml of the third solution was poured into Layer 2 wherein surfaces bounded by Layer 1 formed Layer 3. Then the three-layered membrane was transferred to a vacuum air pump (5×10^{-4} mmHg) for 2 days at room temperature. We selected pure PLGA membrane only, with Layer 1 as control.

2.2. *In vitro degradation*

After 4 h UV light sterilization (30 W, 253.7 nm, DM-5 Navis Cabinet Sterilizer), the rectangular material samples of known weight (Wo) were transferred into tubes filled with 50 ml artificial saliva solution (20 mmol/l $NaHCO_3$, 3 mmol/l NaH_2PO_4 and 1 mmol/l $CaCl_2$, pH 7.4) [25], which were then placed into an incubator. Artificial solution was used instead of the simulated body fluid which specially referred to the oral environment for application, and was more simple for the analysis of the mechanism. The incubator was set as 37 °C. The experiment was conducted for 1, 2, 4, 8 and 12 weeks.

2.3. *Characterization*

At each time interval, samples were removed from the solution, washed with distilled water and air-dried overnight. The overall appearance was recorded by digital camera. The corresponding dry weight (Wt) was recorded prior to further analysis of the samples. The accuracy of the weight measurements is 0.1 mg measured by Electronic Balance (AEG-320, Shimadzu Co. Japan).

$$\text{Weight loss}\,(\%) = \frac{\text{Wo} - \text{Wt}}{\text{Wo} \times 100}$$

At the same time, the pH value of the residual solution was measured using a pH ion meter at room temperature (25 °C, Accuracy ±0.01, IM-55G, Toadkk Co., Japan). The calcium concentration of the residual solution was measured by an Inductively Coupled Plasma Atomic Emission Spectrometer (HITACHI ICP P-4010, Japan). All studies were performed in triplicate. Values are expressed as mean ± standard deviation ($n = 3$). Data were analyzed by t-test with the level of significance set at 5%.

Changes in the two surface morphologies of the membrane during in vitro degradation were evaluated by field emission scanning electron microscopy (FESEM) (Sirion 200, FEI Company, USA) after coating the air-dried samples with gold using an electronic beam (2.5 kV).

3. Results

Fig. 1 revealed the weight loss percentage of the nCHAC/PLGA three-layer membrane and the PLGA one-layer membrane. Almost in the same ratio, the composite membrane is a little slower than the PLGA membrane through the straight linear fit in the 12-week period, and at the 1st and 12th weeks, there were significant differences. At 4 weeks, the average ratio of composite membrane is about 23.1%, while 30.7% for the PLGA membrane. Then until 12 weeks, the average ratio of composite membrane is about 88%, with 98.9% for the PLGA membrane. The main control of this composite for degradation is the polymer component—PLGA. The addition of the nCHAC component would slightly slow the degradation process, but the porous structure of the composite membrane would speed the degradation process. Moreover, the gross appearance of the composite membrane changed over time during degradation as shown in Fig. 2. The initially transparent membrane became whitish due to water absorption. The membranes became more stiff and brittle after placement in the solution. Their bulk shape remained almost intact up to 4 weeks, after that it became powder at the 8th week, and almost nothing at week 12, which corresponded to the result of weight loss during the degradation period in Fig. 1. At 3 months, the three

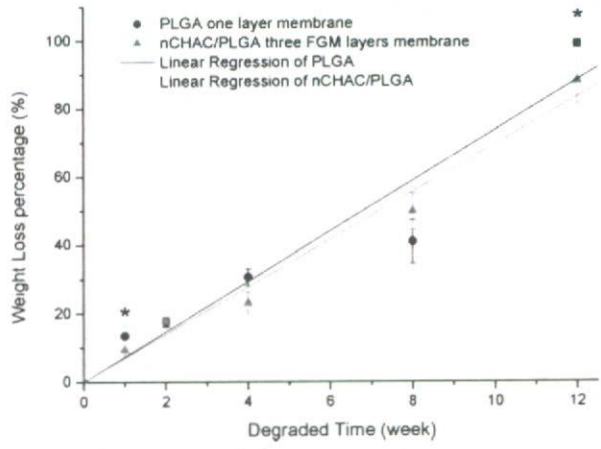

Fig. 1 – The weight loss of the two membranes: nCHAC/PLGA, three FGM layers membrane (linear regression: Y = 6.93367 × X) and pure PLGA one layer membrane (linear regression: Y = 7.35939 × X). The significant difference point between the two membranes was shown as $^{*}P > 0.05$.

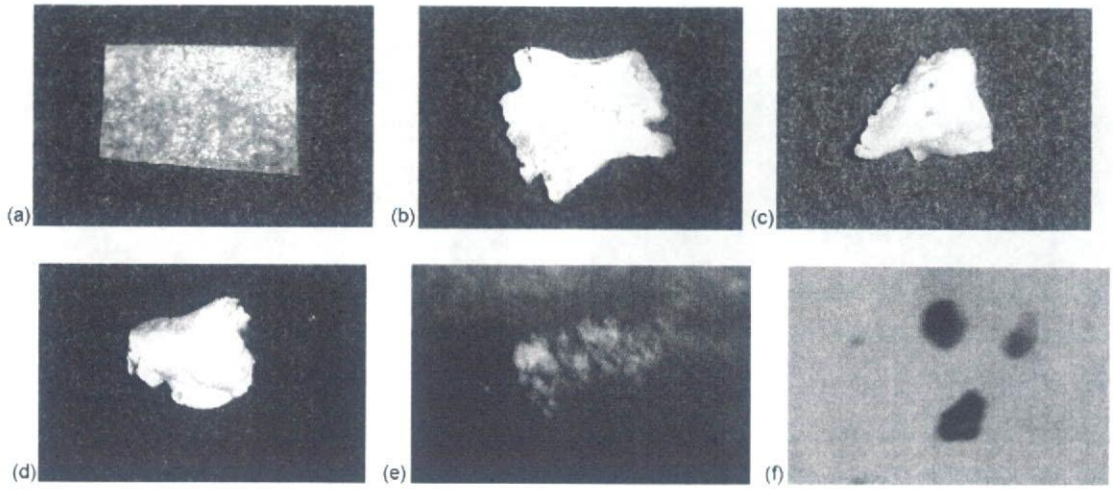

Fig. 2 – The gross appearance of the nCHAC/PLGA composite membrane during degradation: (a) 0 week; (b) 1 week; (c) 2 weeks; (d) 4 weeks; (e) 8 weeks; (f) 12 weeks, 10 mm.

FGM layers nCHAC/PLGA composite membrane were almost completely degraded, which is within the range for periodontal healing.

While in the non-change solution at a different point, it showed significantly different values at 8 and 12 weeks, both for calcium concentration and pH value as shown in Fig. 3. The distinct increase in calcium concentration may refer to the nano-carbonated hydroxyapatite dissolved in the solution, which compares with the no distinct change in the pure PLGA group. The polymer membrane and three-layer composite membrane all became more acidic after 4 weeks. The average pH values of the composite membrane group are a little higher than those of the pure PLGA polymer membrane, although there is no significant difference. Here, after adding the nCHAC composite, it may help to decrease the pH change

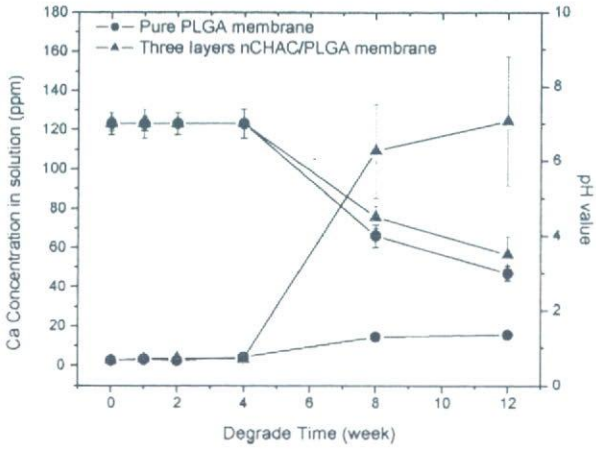

Fig. 3 – The calcium concentration and pH value changes during the degradation of two membranes: nCHAC/PLGA three FGM layers membrane and pure PLGA one layer membrane. The significant difference point between the two membranes is shown as $^{*}P > 0.05$.

in vivo for the body liquid transfers all the time, although no other scientific proof of the nCHA dissolution has been presented to-date.

Then the microstructure changes of the membranes in the whole degradation period were investigated. For the pure PLGA membrane, the micro pore formed in a week with small amounts of debris at 4 weeks, which could be seen by SEM. The pore sizes at 1, 2 and 4 weeks were $0.65 \pm 0.64\,\mu m$, $7.64 \pm 5.86\,\mu m$, $7.70 \pm 5.80\,\mu m$, respectively, from the SEM image calculations ($n = 10$). For the three-layer composite membrane, two different sides of the composite were observed; the side of pure polymer became unsmooth at 1 and 2 weeks (Fig. 4(a and b)). The circle pore then appeared and the quantity of pores is very high as shown in Fig. 4(c). At 4 weeks, the pore became larger and the number of pores increased. For the porous surface of the nCHAC/PLGA side, there were large pores and small pores at micrometer level which appeared in the 1st week (Fig. 5(a)). In the enlarged pore structure, the micro-pores could be detected at nanometer level. The following increased pore size and new pore appearance could be seen (Fig. 5(b and c)). The pore sizes at 1, 2 and 4 weeks of the porous surface of the nCHAC/PLGA side were $(6.7 \pm 3.7) \times 10\,\mu m$, $(9.0 \pm 2.2) \times 10\,\mu m$, $(1.4 \pm 0.2) \times 10^2\,\mu m$, respectively, from the SEM image calculations ($n = 10$). At the same time, the interface between the nCHAC and polymer became porous, not tight (Fig. 6). At 2 weeks, the porous structure was kept on. The polymer on the surface of the nCHAC crystal gradually disappeared. Compared to the 1-week samples, the mineral crystal was seen more clearly and was smaller in size. The combination of nCHAC and polymer changed to a porous scaffold shape. A unique phenomenon appeared on the surface in the 2-week sample (Fig. 7). A hemispheroid and hollow cutting mineral formation consisted of small plate-like, nano-mineral crystals. The authors tentatively suggest this to be nano-apatite crystal, which needs more scientific experimental proof in the future.

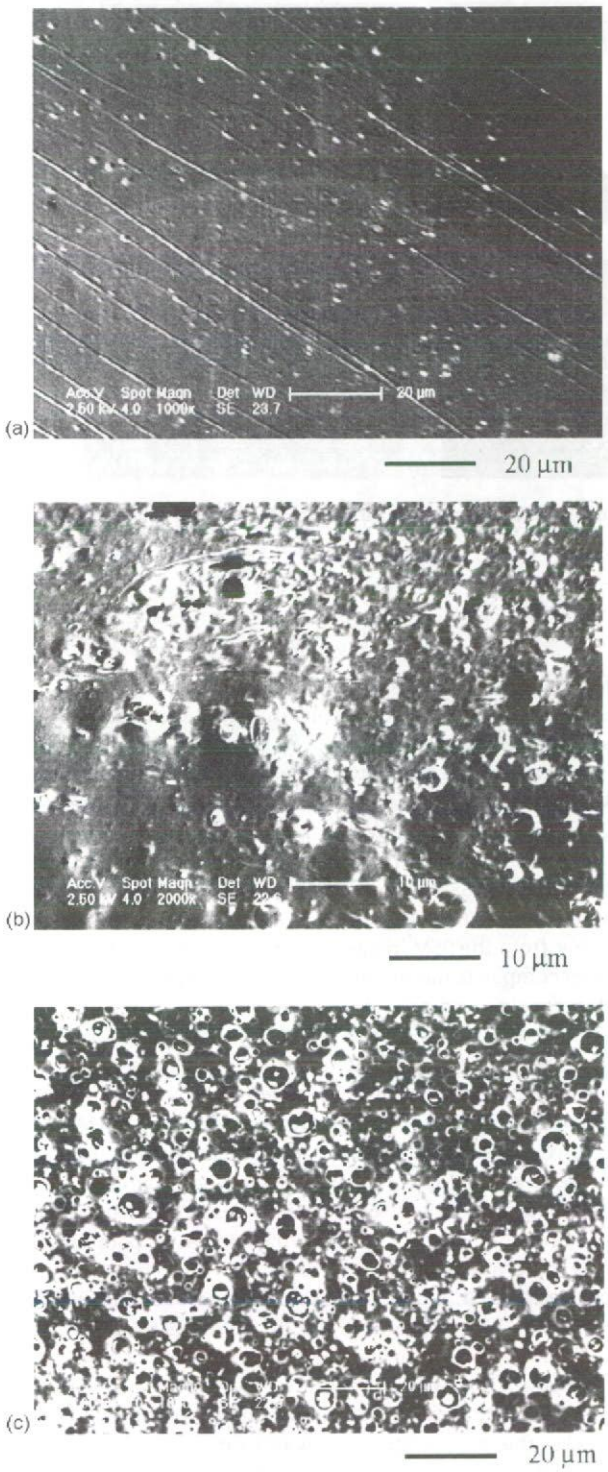

Fig. 4 – The morphological changes of the nonporous side on the nCHAC/PLGA three FGM layer membrane observed by SEM: (a) 1 week; (b) 2 weeks; (c) 4 weeks.

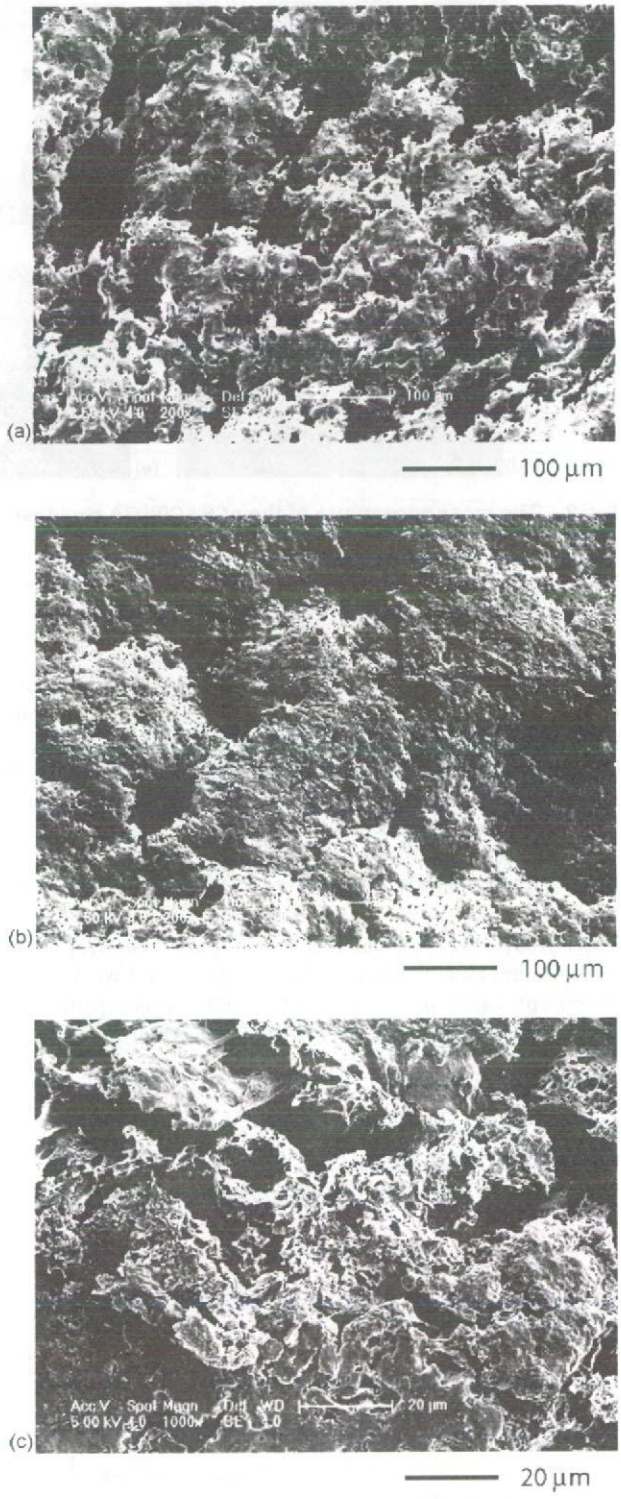

Fig. 5 – The morphological changes of the porous side on the nCHAC/PLGA three FGM layer membrane observed by SEM: (a) 1 week; (b) 2 weeks; (c) 4 weeks.

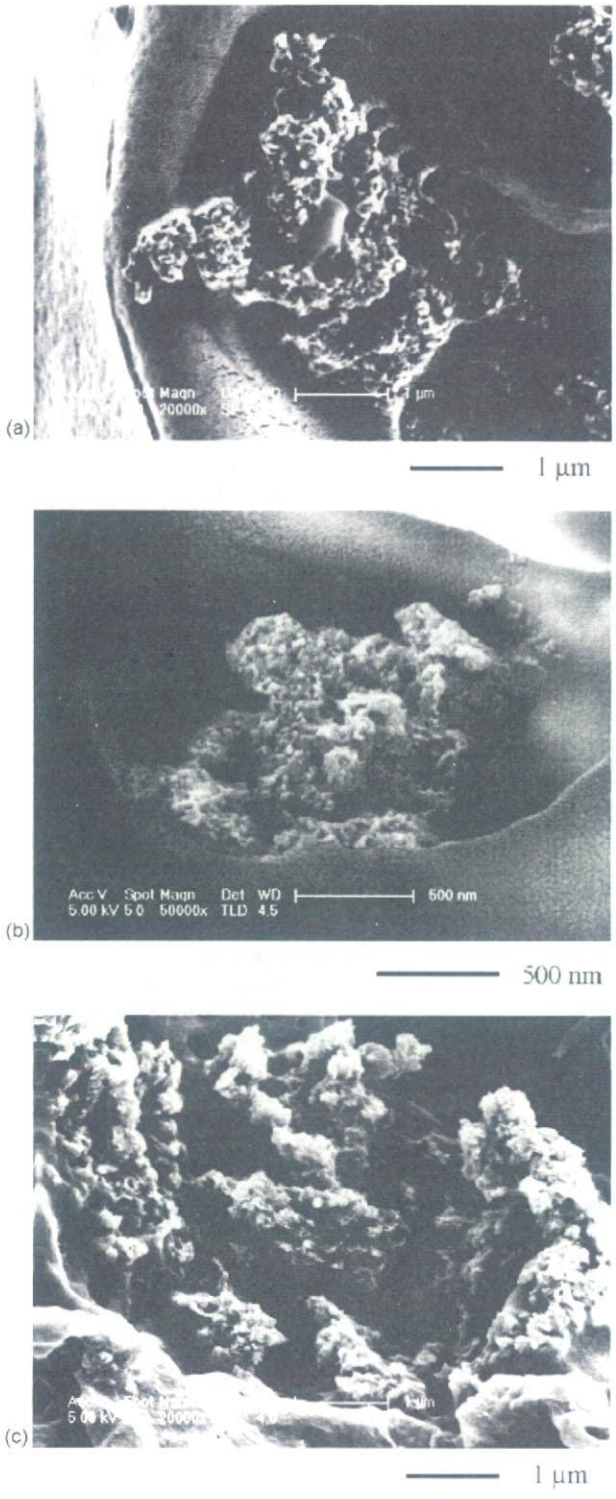

Fig. 6 – The morphological changes of the porous surface on the nCHAC/PLGA three FGM layer membrane observed by SEM: (a) 1 week; (b) 2 weeks; (c) 4 weeks, especially on the nCHAC particles change.

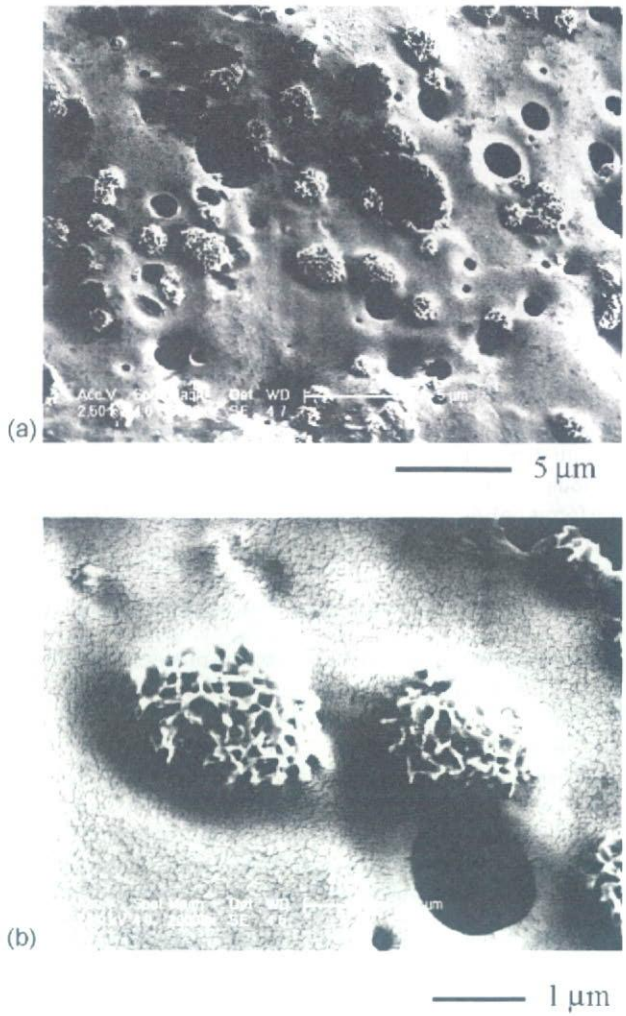

Fig. 7 – The new nano-apatite formation on the porous surface of the nCHAC/PLGA three FGM layer membrane at 2 weeks observed by SEM, (b) enlarged central part of (a).

4. Discussions

This study was designed to measure the changes in sample weight, calcium apatite degradation, pH value and morphology of a new three-layered membrane over a 12-week period of in vitro degradation in artificial saliva solution to determine its possible application for guided tissue regeneration. Specifically, with the addition of nCHAC, positive effects were demonstrated, and the two different surfaces of the membrane showed the different changes in morphology.

The pure PLGA membrane, as control group, took about 12 weeks for full degradation in vitro. This is consistent with results published by other investigators using different specimen configurations. From the research report of Ramchandani et al. [26], the average degradation for PLGA 85:15 was ≈26 weeks and that for PLGA 50:50 was 6–8 weeks, which is the same as early in vivo degradation studies on a series of PLGA copolymers: the degradation ratio was found to increase as PGA < PLA100 < PLA75GA25 < PLA50GA50 < PLA

25GA75 [27,28]. These copolymers were bioabsorbed through hydrolysis returning them to their original components, which are subsequently expelled from, or assimilated into, the body. The in vivo longevity of a particular copolymer is a function of its molecular weight combined with the ratio of its lactide and glycolide components. In general, the rate of hydrolysis decreases with increasing lactic acid imposition. In the current study the PLGA copolymer ratio 75:25, as the main component, was selected for the composite membrane, which can control the potential degradation time of the membrane. With the help of degradation experiments in vitro, the quantitative values for the degradation of this composite were obtained in 12 weeks. The composite maintained the bulk structure throughout the 4-week experimental period, although the weight loss of this membrane was about 23%, which is the essential condition for initial new tissue ingrowth and continuous growth with the following degradation. Compared to the former nHAC/PLA porous scaffold composite for bone substitutes, its in vivo degradation is about 30% in 4 weeks, but only 40% in 10 weeks, which is mainly based on initial degradation of nano-HA crystals and collagen fibrils and the slow degradation ratio of PLA polymer in the later period [29]. From the experimental degradation results, the nCHAC/PLGA three-layered membrane is appropriate for the repair of periodontal defects.

The outcome of PLA or PLGA degradation leads to a decreased pH value in the microenvironment [30,31]. Then the addition of nano-hydroxyapatite/collagen or more easily degraded nano-carbonated hydroxyapatite/collagen in the polymer is favorable for two reasons: first, it increases the bioactivity of the material and second, it compensates for a long-term pH decrease that usually occurs during the degradation of polyesters, the same as Epple's idea on addition of calcium carbonate and calcium phosphate into PLA or PGA polymer [32,33]. In the results of the current study, the slightly neutralizing effect is shown after 4 weeks. The other important factor is the significant increase of calcium concentration in the solution after 4 weeks, which demonstrated that degradation of nano-carbonated hydroxyapatite along the pH value decreased. This biomimetic composite could easily be resorbed by cells and/or dissolved in body fluids because it has a porous structure in one surface and was made of CHA nanocrystals, collagen nano-fibrils and PLGA polymer. Because biodegradable synthetic polymers are relatively hydrophobic, hybridization with collagen or mineralized collagen improved the wettability [34,35]. Due to the good wettability of this composite, the rapid increase in weight loss happened in the first few days. Murphy and Shin et al. [21,36] even reported that the mineralized surface formation on a PLGA scaffold in higher ion concentration simulated body fluid, especially phase size of minerals in 2.00 × SBF is lower than that in 0.75–1.75 × SBF, after 16 days incubation. In agreement with observations in the current study, there is also new mineral formation only on the porous surface of composite membrane at 2 weeks. The plate-like nano-apatite assembled into a half spherical structure, is different to the result of other experiments for mineralized substrates. Whether or not, the high Ca^{2+} and $H_2PO_4^-$ ions play a key role for new mineral formation on the PLGA surface in vitro. The ion source may be very important for bone mineral regeneration in vivo, the possible quick mineral formation at defect sites could be achieved after the composite membrane implantation. Of course, in the future, more intensive research is needed on mineralization in artificial saliva solution.

The special graded structure of the nCHAC/PLGA membrane is one surface that provides an open porous structure of void spaces capable of accommodating tissue ingrowth while the opposite surface of pure PLGA provides a cell-barrier. Changes in the morphology of porous pure PLGA polymer under 40% and 100% humidity was investigated by Kim et al., and the porosity and pore size of the membranes decreased somewhat with time [10]. Moreover, as the composition ratio of lactide to glycolide in the copolymer decreased, the structural changes became severe. While in the current observations of the morphology changes at the pure PLGA surface, nonporous became a distinctly micro-porous structure at the 4th week. Before that time the appearance of the surface is still smooth. For the initial porous surface of the nCHAC/PLGA membrane, the new micro-pores appeared and initial pore size increased during the degradation period. The micrometer level pore size is essential for cellular adaptation and sufficient nutrient permeation [37–39]. The increased porous structure of the membrane is helpful for cell ingrowth and new bone formation. During the increase in pore size, the nano-CHAC/PLGA particles also changed. For the disappearance of the surrounding polymer layer, the nCHAC could directly degrade into the solution, which is in good agreement with the former calcium concentration results.

Current studies showed that the nCHAC/PLGA graded membrane could be some of the most promising materials for guided tissue regeneration for their excellent biocompatibility, biodegradability and availability. Subsequent work is in progress on in vivo degradation plus animal implant experiments. Moreover, in vitro new mineral formation is needed to investigate the mechanism and other aspects in detail in the future, which may help the understanding of in vivo mineralization.

5. Conclusions

The in vitro biodegradation of nano-carbonated hydroxyapatite/collagen/poly(lactic-co-glycolic acid) three-layered membrane was studied. The degradation rate of the composite membrane is a little slower than pure PLGA membrane, but both almost fully degraded in 12 weeks. After 4 weeks, the nano-carbonated hydroxyapatite degradation was caused by the significant increase of calcium concentration in the residue solution. The membrane bulk could be kept for 4 weeks which is essential for supporting sufficient space for periodontal repair in vivo. The pore of 8 wt% nCHAC + PLGA surface was enlarged and increased on the porous surface, while on the nonporous surface of pure PLGA small porous structures also appeared during the increasing degradation period.

Acknowledgements

This research was funded by JSPS (Japan Society for the Promotion of Science). Thanks for Dr. Hiroko Takita (Hokkaido

University, Graduate School of Dental Medicine) for freezing-dry samples. Thanks for Professor Yoshinori Kuboki (Hokkaido University, Graduate School of Dental Medicine) and Professor Matthias Epple (University of Duisburg-Essen, Institute of Inorganic Chemistry) who gave us helpful discussions.

REFERENCES

[1] Lu L, Mikos AG. The importance of new processing techniques in tissue engineering. Mater Res Soc Bull 1996;21:28–32.
[2] Witt C, Mader K, Kissel T. The degradation, swelling and erosion properties of biodegradable implants prepared by extrusion or compression moulding of poly(lactide-co-glycolide) and ABA triblock copolymers. Biomaterials 2000;21:931–8.
[3] Thomoson RC, Mikos AG, Beahm E, Lemon JC, Evans GRD, Sufdemorte TB, et al. Guided tissue fabrication from periosteum using preformed biodegradable polymer scaffolds. Biomaterials 1999;20:2007–18.
[4] Wider MS, Gupta PK, Lu L, Meszlenyi RK, Evans GRD, Brandt K, et al. Manufacture of porous biodegradable polymer conduits by an extrusion process for guided tissue regeneration. Biomaterials 1998;19:1945–55.
[5] Ashammakhi N, Rokkanen P. Absorbable polyglycolide devices in trauma and bone surgery. Biomaterials 1997;18:3–9.
[6] Osther PJ, Gjode P, Mortensen BB, Bartholin J, Gottrup F. Randomized comparison of polyglycolic acid and polyglyconate sutures for abdominal fascial closure after laparotomy in patients with suspected impaired wound healing. Br J Surg 1995;82:1080–2.
[7] Ishaug-Riley SL, Crane GM, Gurlek A, Miller MJ, Yasko AW, Yaszemski MJ, et al. Ectopic bone formation by marrow stromal osteoblast transplantation using poly(DL-lactid-co-glycolic acid) foams implanted into the rat mesentery. J Biomed Mater Res 1997;36:1–8.
[8] Langer R. Drug delivery and targeting. Nature 1998;392(Suppl.):5–10.
[9] Lu L, Garcia CA, Mikos AG. In vitro degradation of thin ploy(DL-lactic-co-glycolic acid) films. J Biomed Mater Res 1999;46:236–44.
[10] Kim SY, Kanamori T, Noumi Y, Wang PC, Shinbo T. Preparation of porous poly(DL-lactide) and poly(DL-lactide-co-glycolide) membranes by a phase inversion process and investigation of their morphological changes as cell culture scaffolds. J Appl Polym Sci 2004;92:2082–92.
[11] Du C, Cui FZ, Zhu XD, de Groot K. Three-dimensional nano-HAp/collagen matrix loading with osteogenic cells in organ culture. J Biomed Mater Res 1999;44:407–15.
[12] Zhang W, Liao SS, Cui FZ. Hierarchical self-assembly of nano-fibrils in mineralized collagen. Chem Mater 2003;15:3221–6.
[13] Liao SS, Cui FZ, Zhang W, Feng QL. Hierarchically biomimetic bone scaffold materials: nano-HA/collagen/PLA composite. J Biomed Mater Res Part B (Appl Biomater) 2004:158–65.
[14] Liao SS, Cui FZ, Zhu Y. Osteoblasts adherence and migration through three-dimensional porous mineralized collagen based composite: nHAC/PLA. J Bioact Comp Poly 2004;19:117–30.
[15] Liao SS, Guan K, Cui FZ, Shi SS, Sun TS. Lumbar spinal fusion with a mineralized collagen matrix and rhBMP-2 in a rabbit model. Spine 2003;28:1954–60.
[16] Liao SS, Watari F, Uo M, Ohkawa S, Tamura K, Wang W, et al. The preparation and characteristics of a carbonated hydroxyapatite/collagen composite at room temperature. J Biomed Mater Res Part B (Appl Biomater) 2005;74B:817–21.
[17] Schanek WJ, Yoshimura M. Processing and properties of hydroxyapatite-based biomaterials for use as hard tissue replacement implants. J Mater Res 1998;13:94–117.
[18] Doi Y, Shibutani T, Moriwaki Y, Kajimoto T, Iwayama Y. Sintered carbonate apatites as bioresorbable bone substitutes. J Mater Res 1998;39:603–10.
[19] LeGeros RZ. Calcium phosphates in oral biology and medicine. Basel, Switzerland: Karger AG; 1991.
[20] Kokubo T, Kushitani H, Abe Y. Apatite coating on various substrates in simulated body fluids. Bioceramics 1989;2:235–42.
[21] Murphy WL, Mooney DJ. Bioinspired growth of crystalline carbonate apatite on biodegradable polymer substrata. J Am Chem Soc 2002;124:1910–7.
[22] Kim HM, Himeno T, Kokubo T, Nakamura T. Process and kinetics of bonelike apatite formation on sintered hydroxyapatite in a simulated body fluid. Biomaterials 2005;26:4366–73.
[23] Kokubo T. Formation of biologically active bone-like apatite on metals and polymers by a biomimetic process. Thermochim Acta 1996;280/281:479–90.
[24] Liao SS, Wang W, Uo M, Ohkawa S, Aksaka T, Tamura K, et al. A three-layered nano-carbonated hydroxyapatite/collagen/PLGA composite membrane for guided tissue regeneration. Biomaterials 2005;26:7564–71.
[25] Birkeland JM. The effect of pH and the interaction of fluoride and salivary ions. Carries Res 1993;7:11–8.
[26] Ramchandani M, Pankaskie M, Robinson D. The influence of manufacturing procedure on the degradation of poly(lactide-co-glycolide) 85:15 and 50:50 implants. J Control Release 1997;43:161–73.
[27] Miller RA, Brady JM, Cutright DE. Degradation rates of oral resorbable implants (polylactates and polyglycolates): rate modification with changes in PLA/PGA copolymer ratios. J Biomed Mater Res 1977;11:711–9.
[28] Kister G, Cassanas G, Vert M. Structure and morphology of solid lactide-glycoide copolymers from ^{13}C NMR, infra-red and Raman spectroscopy. Polymer 1998;39:3335–40.
[29] Liao SS, Cui FZ. In vitro and in vivo degradation of the mineralized collagen based composite scaffold: nanohydroxyapatite/collagen/poly(L-lactide). Tissue Eng 2004;10:73–80.
[30] Ishaug SL, Crane GM, Miller MJ. Bone formation by three-dimensional stromal osteoblast culture in biodegrable polymer scaffolds. J Biomed Mater Res 1997;37:17–28.
[31] Agrawal CM, Athanasiou KA. Technique to control pH in vicinity of biodegrading PLA-PGA implants. J Biomed Mater Res 1997;38:105–14.
[32] Schiller C, Rasche C, Wehmoller M, Bechmann F, Eufinger H, Epple M, et al. Geometrically structured implants for cranial reconstruction made of biodegradable polyesters and calcium phosphate/calcium carbonate. Biomaterials 2004;25:1239–47.
[33] Linhart W, Peters F, Lehmann W, Schwarz K, Schiling AF, Amling M, et al. Biologically and chemically optimized composite of carbonated apatite and polyglycolide as bone substitution materials. J Biomed Mater Res 2001;54:162–71.
[34] Chen GP, Ushida T, Tateishi T. Development of biodegradable porous scaffolds for tissue engineering. Mater Sci Eng C 2001;17:63–9.
[35] Mikos AG, Lyman MD, Freed LE, Langer R. Wetting of poly(L-lactic acid) and poly(DL-lactic-co-glycolic acid) forms for tissue culture. Biomaterials 1994;15:55–8.
[36] Shin K, Jayasuriya AC, Luong L, Outslay M, Kohn DH. Formation and dissolution behavior of biomimetic mineral

on 3-dimensional poly(lactide-co-glycolid) scaffold. In: Proceeding of the 7th world biomaterials congress. 2004. p. 1841.
[37] Tancred DC, McCormack BAO, Carr AJ. A synthetic bone implant macroscopically identical to cancellous bone. Biomaterials 1998;19:2303–11.
[38] Middleton JC, Tipton AJ. Synthetic biodegradable polymers as orthopedic devices. Biomaterials 2000;21:2335–46.
[39] Jain RA. The manufacturing techniques of various drug loaded biodegradable poly(lactide-co-glycolide) (PLGA) devices. Biomaterials 2000;21:2475–90.

Available online at www.sciencedirect.com
ScienceDirect
Acta Biomaterialia 3 (2007) 669–675
Acta BIOMATERIALIA
www.elsevier.com/locate/actabiomat

Self-assembly of nano-hydroxyapatite on multi-walled carbon nanotubes

Susan Liao [a,b,*], Guofu Xu [c], Wei Wang [d], Fumio Watari [d], Fuzhai Cui [e], Seeram Ramakrishna [a,f], Casey K. Chan [a,b]

[a] *Nanoscience and Nanotechnology Initiative, Division of Bioengineering, Faculty of Engineering, National University of Singapore, Singapore 117576, Singapore*
[b] *Department of Orthopaedic Surgery, Yong Loo Lin School of Medicine, National University of Singapore, Singapore 119074, Singapore*
[c] *School of Materials Science and Engineering, Central South University, Changsha 410083, China*
[d] *Graduate School of Dental Medicine, Hokkaido University, Sapporo 060-8586, Japan*
[e] *Department of Materials Science and Engineering, Tsinghua University, Beijing 100084, China*
[f] *Department of Mechanical Engineering, Faculty of Engineering, National University of Singapore, Singapore 117576, Singapore*

Received 3 October 2006; received in revised form 9 March 2007; accepted 16 March 2007
Available online 18 May 2007

Abstract

Inspired by self-assembly of nano-hydroxyapatite (nHA) on collagen associated with the 67 nm periodic microstructure of collagen, we used multi-walled carbon nanotubes (MWCNTs) with approximately 40 nm bamboo periodic microstructure as a template for nHA deposition to form a nHA–MWCNT composite. The assembled apatite was analyzed by transmission electron microscopy and scanning electron microscopy. Defects that were analogous to edge dislocations along the carbon nanotubes' multi-walled surfaces were the nucleation sites for nHA after these defects had been functionalized principally into carboxylic groups. Spindle-shaped units consisting of an assembly of near parallel, fibril-like nHA polycrystals were formed and oriented at a certain angle to the long axis of the carbon nanotubes, unlike nHA–collagen in which the nHA is oriented along the longitudinal axis of the collagen molecule. One possible explanation for this difference is that there are more bonds for calcium chelation (–COOH, >C=O) on the collagen fibril surface than on the surface of MWCNTs. Spindle-shaped units that are detached from the MWCNT template are able to maintain the ordered parallel structure of the nHA polycrystal fibril. We have thus created a self-assembled hydroxyapatite on MWCNTs.

Keywords: Carbon nanotubes; Nano-hydroxyapatite; Bioinspired; Self-assembly; Collagen

1. Introduction

Various models have been designed to simulate the collagen mineralization process from the gene to the peptide level using a range of materials from natural extracellular matrix to synthetic polymers. Such investigations aim to study the basic mechanisms of biomineralization. Moreover, insights and understanding of these mechanisms will enable better design and fabrication strategies for nanocomposites to be used for hard tissue (bone and teeth) repair and replacement [1–8]. Zhang focused on fabricating self-assembling peptides and protein nanofibers. He showed that surfactant-like peptides (~2 nm in size) could self-assemble into nanotubes with a diameter of ~30–50 nm, which then formed an interconnected network similar to that observed in carbon nanotubes [3]. Stupp and colleagues developed a peptide–amphiphile model to study the self-assembly and mineralization mechanisms.

* Corresponding author. Address: Nanoscience and Nanotechnology Initiative, Division of Bioengineering, Faculty of Engineering, National University of Singapore, Singapore 117576, Singapore. Tel.: +65 65164272; fax: +65 67730339.
E-mail address: bieliaos@nus.edu.sg (S. Liao).

1742-7061/$ - see front matter © 2007 Acta Materialia Inc. Published by Elsevier Ltd. All rights reserved.
doi:10.1016/j.actbio.2007.03.007

After cross-linking the peptide–amphiphile fibers, Stupp et al. were able to direct mineralization of hydroxyapatite (HA) to form a composite material in which the crystallographic *c*-axes of HA were aligned along the long axes of the fibers. This alignment is similar to that observed between collagen fibrils and HA crystals in natural bone [4]. However, this model does not simulate higher-level assembly. Because the micro–macro hierarchical structure is not modeled, it is not possible to infer realistic gross mechanical properties.

Since the discovery of fullerenes and carbon nanotubes, the unique structure-dependent electrical and mechanical properties of carbon structures have been the subject of extensive research [9]. Potential applications include nanodevices, nanosensors, ultra-high-strength engineering fibers, etc. To optimize the use of carbon nanotubes (CNTs) in these applications, a number of strategies have also been developed for the surface modification of CNTs by functional groups and functional-group-anchored nanoparticles [10–12]. It has demonstrated that open-ended single-walled carbon nanotubes (SWCNTs) can be solubilized in organic solvents, and can be further derivatized by the adsorption of hydroxystilbene fluorophore onto the carbon surface via ester coupling [12]. Mixed-monolayer-protected Au clusters can be strongly adsorbed onto the carbon surface. SWCNTs that are prepared via alumina-membrane synthesis and filled Pt/Ru nanoparticles can act as an electrocatalyst for methanol oxidation and oxygen reduction [13]. Han et al. reported a simple and effective method for preparing alkanethiolate monolayer-capped gold nanoparticles on multi-walled carbon nanotubes (MWCNTs) by molecularly mediated assembly [14]. In yet another demonstration of the self-assembly capability of CNTs, Rosca et al. [15] and Li et al. [16] showed that after prolonged nitric acid oxidation, the fragmented MWCNTs aligned themselves into areas of parallel nanotubes, and had the tendency to self-organize into aligned nanotube ribbons. There has also been a tremendous interest in taking advantage of the unique properties of CNTs for promising biological applications. MWCNTs are capable of being shaped into three-dimensional (3-D) architectures, giving rise to the possibility of using this material as a new form of scaffold for tissue engineering [17]. In view of the high surface area/volume ratio, structure periodicity and molecular affinity, we studied the feasibility of using MWCNTs as a template for the fabrication of assembled nanohydroxyapatite (nHA). A comparison of the mechanism of mineralization of this template with the mineralization of collagen fibers may help develop a more rational design strategy for biomimetic materials for hard tissue repair. We hypothesize that the unique microstructure of certain MWCNTs with bamboo periodicity can direct the nanosized apatite assembly via an aqueous solution reaction. The dislocations on the surface of these CNTs can serve as sites for nucleation of HA after the MWCNTs are functionalized by carboxyl groups or other groups for calcium chelation [15,18–20]. We also compare the mechanism of in vitro mineralization of the collagen fibril unit with that of CNTs with and without carbonate. By studying the capability of CNTs to promote assembly and mineralization, it is possible to gain insights in new self-assembling mineralization systems.

2. Materials and methods

Non-carbonated nHA and carbonated nHA were prepared for comparative studies using MWCNTs and collagen as nucleation templates. MWCNTs with bamboo structures provided by Nanolab Inc. (USA) as shown in Fig. 1a were grown by chemical vapor deposition. They have a diameter of 20–40 nm, and an average length of 5.0 μm. The purification procedure for MWCNTs was as follows: First, MWCNTs were heated to approximately 773 K for 90 min under atmospheric conditions. Next, the cooled MWCNTs were transferred into a flask containing 6 M HCl and treated at 333 K for 2 h to remove residual metals and metal oxides. The acid solution was filtered using a polytetrafluoroethylene membrane filter with a pore size of 0.2 μm. The filtered cake was rinsed out with double-distilled water and subsequently dried at 333 K for 12 h.

The above-purified MWCNTs were added to 0.5 M acetic acid. Solutions of 0.5 M $CaCl_2$ and 0.5 M H_3PO_4 (Ca/P = 1.66) were gradually added through separate tube pumps and the mixture stirred for 1 h. The mixture was then separated into two equal portions. A solution of Na_2CO_3 (molar ratio of $CO_3^{2-}/PO_4^{3-} = 3$) was gradually added to one of these portions. Both portions were stirred for 30 min, and then titrated with sodium hydroxide to pH 9 at room temperature [21]. After aging the solution for 2 h, two types of materials, namely nHA/MWCNTs (nHAM) and nano-carbonated HA/MWCNTs (nCHAM) were harvested from each of the portions by centrifugation and freeze-drying.

The above process was repeated with type I atelocollagen gel (2 wt.%, Koken Company, Japan) to make nHA/collagen (nHAC) and nano-carbonated HA/collagen (nCHAC) in a similar manner.

X-ray diffraction (XRD) analysis was performed in a Rigaku/Multiflex diffractometer using Ni-filtered Cu Kα radiation, in the 2θ range of 10°–80° at a scan rate of 2° min^{-1}, with a sampling interval of 0.02°. Data were analyzed by the accompanying MDI JADE6 software [22]. The diffraction peak broadening due to small crystallites can be semi-quantitatively estimated from the Scherrer equation: $\beta_{1/2} = (K\lambda)/(D\cos\theta)$ [23]. $\beta_{1/2}$ is the full-width at half maximum in 2θ and this is automatically calculated by the MDI JADE6 software. K is a constant that we set to 1, λ is the X-ray wavelength in Angstroms, D is roughly the average crystallite size and the θ is the diffraction angle of the corresponding reflex.

A Raman spectrometer (Dilor Jobin Yvon Spex, Group Horiba) was also used to evaluate the samples.

The carbonated weight percentages were measured using thermogravimetric analysis (TGA) (Rigaku Thermoflex

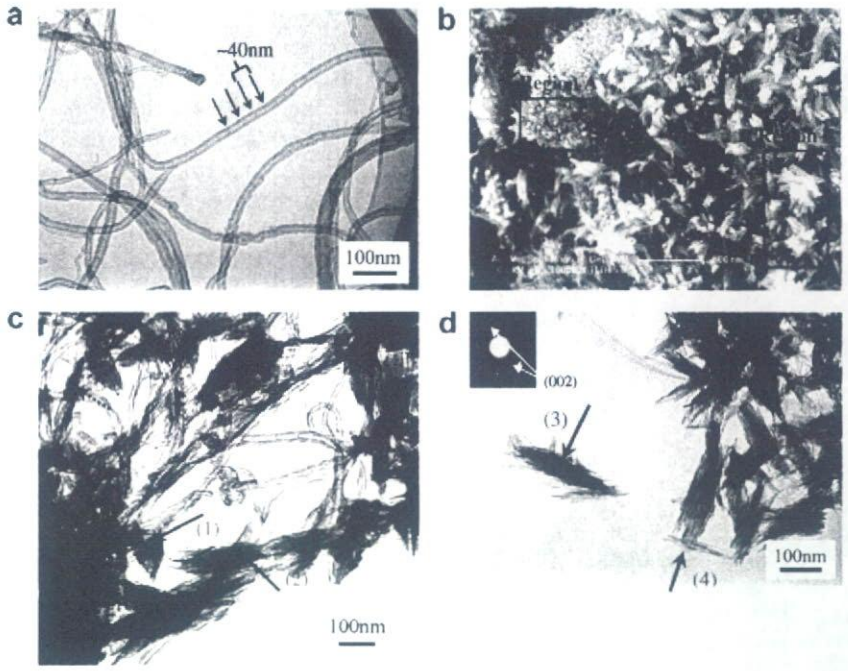

Fig. 1. (a) TEM of nanoscale bamboo structure in MWCNTs. The periodic structure of the bamboo is about 39.6 ± 11.8 nm ($n = 5$). (b) SEM micrographs of nHAM. The spindle unit is about 300 nm long. (c) Network of MWCNTs with nHA shown in region A of (b). Arrows 1 and 2 refer to the nHA attached to MWCNTs, arrow 2 denotes a relatively large nHA spindle unit. Dashed arrows refer to a small nHA spindle unit. (d) TEM analysis of area corresponding to region B in (b). Arrow 3 shows assembly of pure nHA and arrow 4 shows a small spindle unit of nHA. Arrows 2 and 3 indicate the same level spindle unit of nHA crystals. SAED of arrow 3 referring to a bundle of apatite is shown at the top left corner. This SAED demonstrates the orientation of the nHA phase.

TG8110/TAS100). Samples were heated at room temperature to a maximum temperature of 1000 °C at a heating rate of 10 °C min^{-1}. As in natural bone, the weight percentage of water content, organic material (mostly collagen), carbonated apatite and residual mineral (calcium phosphate) of the sample can be determined by the three stages of weight loss during the heating process [24,25].

To prepare samples for transmission electron microscopy (TEM), a drop of the aged reaction solution prior to the freeze-drying step was placed on a carbon film-supported copper grid. After air-drying, the sample was observed on a Hitachi-800 microscope at 150 kV. The freeze-dried samples after gold coating were observed by field emission scanning electron microscopy (FESEM) (Sirion 200, FEI Company, Delaware, USA).

3. Results

The periodic length of a typical MWCNT is approximately 40 nm (Fig. 1a). SEM micrograph observations (Fig. 1b) showed that assembled nHA was associated with MWCNTs. In general, the nHA was self-assembled into spindle-shaped units (Fig. 1b–d) of varying sizes. For example, the spindle-shaped units in region A of Fig. 1b are much smaller than the spindle-shaped units in region B. It is also observed that those spindle-shaped units that are still attached to MWCNTs (dashed arrow in Fig. 1c) are smaller than those that are detached from the MWCNTs (Fig. 1d, arrow 3). Occasionally, smaller spindle-shaped units were observed to be detached from MWCNTs (Fig. 1d, arrow 4). Selected area electron diffraction (SAED) of the apatite domain (Fig. 1d, arrow 3, referring to the apatite bundle) revealed that the spindle-shaped units were oriented in the same direction as the *c*-axes of nHA. This is highly suggestive that the spindle-shaped units are formed from an assembly of near-parallel nHA polycrystal fibril. In general, the spindle-shaped units that are detached from MWCNTs are larger than those spindle-shaped units that are still attached to MWCNTs. The initiation and crystallization phases are continuous processes, which start and terminate randomly at the different sites, and result in spindle-shaped units that vary in size from different regions depending on the local conditions. The detached spindle-shaped units are not only larger but also tend to be more uniform in size.

In this case, the spindle-shaped units tend to orient at an angle of 45° (44.8 ± 3.2°, $n = 5$) with respect to the longitudinal axis of the MWCNTs (Fig. 2a and b). The HRTEM image of the HA crystal on the surface of the MWCNTs revealed an apatite lattice spacing of 0.344 nm, corresponding to the (002) lattice plane of HA (Fig. 2b). As such, the angle between the MWCNT longitudal direction (white arrow) and the formed nHA *c*-axis (black arrow of crystal 1) was about 45° in this position. The three nHA crystals (1, 2 and 3) in Fig. 2b indicated that each nHA fibril was in a polycrystalline phase consisting of many connected small nHA crystals (Fig. 2a). Crystals 2 and 3 showed different directions to crystal 1 as denoted by the black

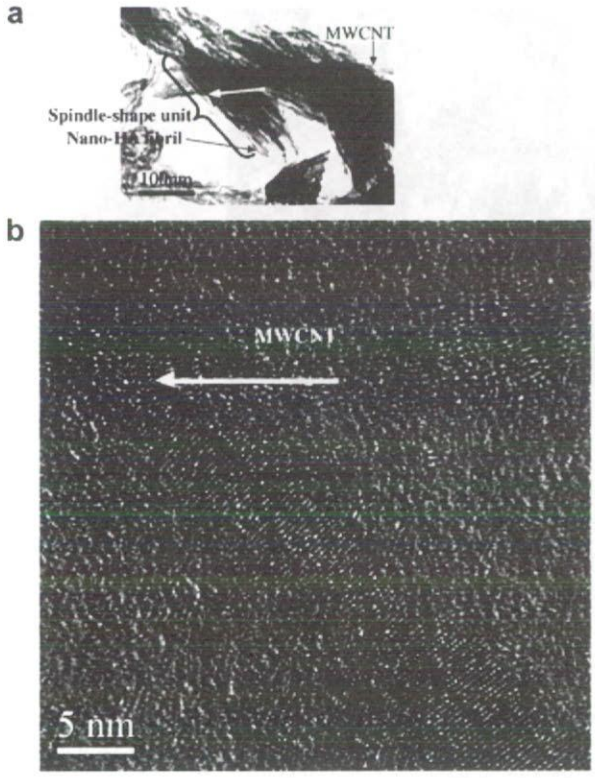

Fig. 2. Directional relationship of nHA and MWCNTs. HA polycrystal fibrils are arranged in parallel to form spindle-shape units that are oriented at an angle relative to the longitudinal axis of CNTs. The white arrow refers to the longitudinal direction of the MWCNTs; the black arrow refers to the orientation of the long axis of nHA [002]. (a) TEM image from Fig. 1c. (b) HRTEM image of nHA/MWCNT. The crystal lattice spacing was 0.344 nm, corresponding to the (002) surface of HA. The angle between the nHA and the MWCNTs was about 45°. Nos. 1, 2 and 3 indicate three HA nanocrystals, as part of a nHA polycrystal fibril.

arrows. This interpretation is also consistent with the typical SAED pattern in Fig. 1d.

A comparison between nHA derived from collagen templates and those derived from MWCNT templates revealed that low-level assemblies consisting of spindle-shaped units were similar in size and shape (Fig. 3a and b). Typically, these spindle-shaped units are more than 300 nm in length and about 60 nm in width. This microstructure may be due to the over-growth of HA on the templates (collagen or MWCNTs) provided that there is sufficient space for continuous growth.

Carbonate can be incorporated into nHA using the biomimetic method described here. The XRD spectra (Fig. 4) showed that all four materials (nHAC, nHAM, nCHAC and nCHAM) were nHA, except for nHAM, which contained micrometer levels of brushite impurities. Brushite is not usually seen when collagen is used as a template because the abundance of nucleation sites and the spatial structure of collagen molecules limit excess growth of nHA and brushite formation. Using software to calculate the peak of [002] in the X-ray data spectra, the average crystal size of each material (nHAM, nCHAM, nHAC, nCHAC) was 41.93 ± 4.70, 16.32 ± 2.92, 26.61 ± 16.33 and 11.61 ± 0.52 nm, respectively. Without the addition of carbonate during preparation, nHAM and nHAC both produced an apatite phase that was larger than those in nCHAM and nCHAC. This is consistent with the TEM observations. From the TEM results (data not shown), the carbonated nHA in nCHAC and nCHAM in general are less than 100 nm in length. The carbonated nHA

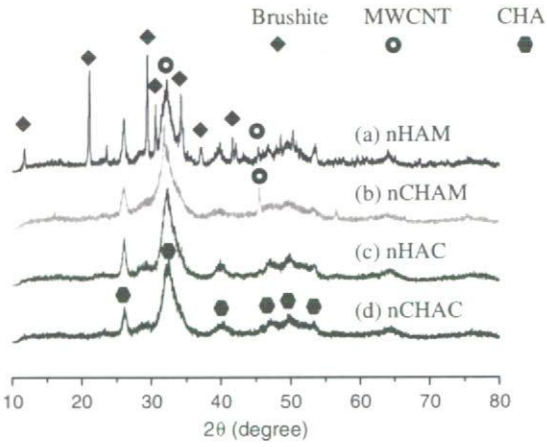

Fig. 4. XRD spectra of (a) nHAM, (b) nCHAM, (c) nHAC and (d) nCHAC. Except for (a), the others are nano-carbonated HA phase without any impurities. (a) is nano-carbonated HA with brushite. From the calculation of the peak of [002] in the spectra, the HA average crystal size for each material was 41.93 ± 4.70, 16.32 ± 2.92, 26.61 ± 16.33 and 11.61 ± 0.52 nm, respectively. The carbonated HA phases in (b) and (d) were both smaller than those of (a) and (c).

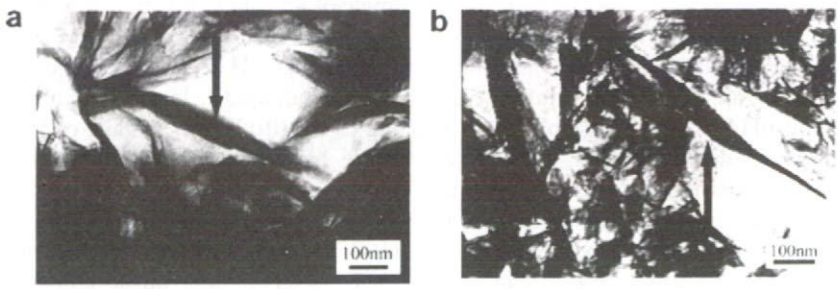

Fig. 3. Spindle-shaped units of apatite co-precipitated with (a) collagen and (b) MWCNTs are of similar size. Each unit is greater than 300 nm in length and 60 nm in width.

(nCHAC and nCHAM) is relatively smaller than the non-carbonated nHA (nHAC and nHAM). In addition to reducing crystal size, carbonation also causes a reduction in tendency to self-assemble into spindle-shaped units, especially when mineralization is carried out with MWCNTs. As a result, only a few of the nCHAC polycrystal fibrils were oriented in a parallel fashion, and in nCHAM there was no distinctive parallel orientation of the polycrystal fibrils. TGA results showed that the carbonate content found in the four materials (nHAM, nCHAM, nHAC, nCHAC) was 4.9%, 7.1%, 4.8% and 7.1%, respectively. The detection of carbonate in nHAM and nHAC is probably due to the absorption of atmospheric carbonate during the preparation process. These results also mean that a slight increase in carbonate content in the composites is associated with a significant decrease in the crystal size regardless of the type of template used.

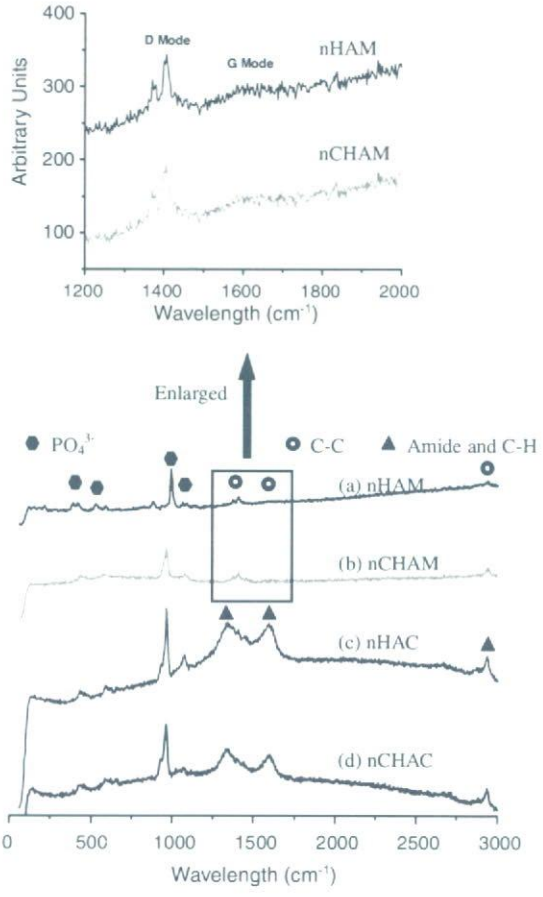

Fig. 5. Raman Spectra of (a) nHAM, (b) nCHAM, (c) nHAC and (d) nCHAC. After replacing MWCNT with collagen, the distinct peaks of amide and C–H were seen. Phosphate was seen in all four spectra, but the phosphate bands in (c) and (d) were higher than those in (a) and (b). In the enlarged portion of (a) and (b), D and G modes are indicated in the upper part of spectra. This is a significant D-mode peak consisting of two sub-peaks. Comparing D-mode peaks of (a) and (b), peaks did not shift significantly (about 1405.775–1370.592 cm^{-1}), and hence this was assigned as the disorder-induced D mode. The D-mode peak is attributed to a finite particle size effect or lattice distortion, such as defects in the curved graphite sheets, tube ends or bamboo structures. On the other hand, the G mode in the two spectra did not show any significant peaks, which is a characteristic of graphite sheets.

In order to detect the interaction between the templates and nHA, we compared the four composites by Raman spectroscopy (Fig. 5). In the enlarged portion of the graph for nHA prepared with MWCNTs, the D and G modes are shown. The D mode has a significant peak, which is made up of two sub-peaks. Comparing the D mode of nHAM and nCHAM, there was no significant shift in the peaks (from 1406 to 1370 cm^{-1}), and hence this was assigned as the disorder-induced D mode. The D-mode peak is attributed to a finite particle size effect or lattice distortion, such as defects in the curved graphite sheets, tube ends or finite size crystalline domains in the nanotubes (nanobells or bamboo structures), etc. [26,27]. The G mode in both spectra occurred at about 1600 cm^{-1}. The G mode also did not display any obvious peaks, which is a characteristic of graphite sheets. However, after replacing MWCNT templates with collagen, distinct peaks of amide and C–H were observed in the spectra.

4. Discussion

It is demonstrated that nucleation and growth of nHA can be initiated by MWCNTs. Raman spectra of nHAM revealed large quantities of surface defects around the MWCNTs. HRTEM of MWCNTs reveals a class of defects analogous to edge dislocation in a crystal [28]. These defects are sites for nucleation and growth of nHA crystals. We suspect that when the aggregations of nHA polycrystal fibril forming the spindle-shaped units reach a sufficient size, these spindle-shaped units become more susceptible to detachment from the MWCNTs. Such speculation is consistent with the observation that detached spindle-shaped units tend to be larger. As a result, we postulate that once the spindle-shaped units have reached a sufficient size, they are detached from the MWCNTs, possibly due to the agitation from stirring, and once detached, the assembly process terminates.

Some investigators reported that several weeks are required for sufficient mineralization to occur if simulated body fluid (SBF) or modified SBF is used [8,29]. There is no apatite formation with CNTs using standard SBF or PBS unless F ions are added and the phosphate concentration is increased [30]. These findings are analogous to our experience that CNTs are not as strong a template as collagen in inducing formation of nHA crystals. However, in the method described here, using a mixture of calcium, phosphate and carbonated ions, mineralization can be achieved in less than a day.

In natural bone, collagen fibrils consist of self-assembled collagen triple helices. Along the long axis of collagen, the quarterly staggered pattern produces a 67 nm long periodic structure with 40 nm hole and 27 nm folded part. The holes provide sites for mineral nucleation and growth. Minerals assemble along the long axis and contiguous channels allow for the creation of 3-D layers in natural mineralized

tissue [1,2,31]. Our previous in vitro collagen mineralization experiment showed that HA crystals could also nucleate and grow on the surface of collagen fibrils. Previous studies have proven that the negatively charged carboxyl and carbonyl groups found in collagen molecules can act as nucleation sites for HA crystals [32]. This is because oxygen in the hydroxyl group of HA has an epitaxial relationship with the carboxyl groups of collagen. Furthermore, HA crystals covering the surface of collagen fibrils were observed to have their *c*-axes aligned along the longitudinal axes of collagen fibrils. These mineralized collagen bundles were assembled from parallel collagen fibers with calcium phosphate crystals on their surfaces. In an analogous manner, physical and chemical treatments can be employed to align HA crystals. One such method is to add carboxyl or carbonyl functional groups to CNTs so that CNTs possess both structural compatibility and chemical complementarity for mineral formation. Based on such a complimentary and directional relationship between CNTs and apatite, a novel method was used to induce apatite assembly. We speculate that compared to collagen, MWCNTs are a less ideal template for nucleation and growth of the nHA and, as a result, brushite is formed as a by-product. This undesirable by-product can be eliminated by the addition of carbonate. In addition to the special spatial structure of the CNT surface, it is possible that the oxidation of the CNT surface to carboxylic group can also enhance the nucleation of nHA. Comparison of the relative peak ratio in the Raman spectra has shown that MWCNTs contribute about 0.18 wt.% to the composites, and this is much lower than the collagen content (16.5 wt.%) for composites using collagen as a template. Despite the small percentage of templates, MWCNTs are a productive template for HA crystal formation. This is due to their large surface area (220 $m^2 g^{-1}$) with abundant defects acting as mineral nucleation sites for HA crystallization. Moreover, the 40 nm periodic bamboo structure provides the periodic defect structure on the surface of CNTs for nucleation sites of HA. In this study, we control the size of formed HA by controlling the time of the reaction. If MWCNTs are further assembled into an aligned array, the space between parallel CNTs will limit the over-growth of HA, as occurs in the collagen assembly of natural bone tissue. The hierarchical assembly of MWCNTs with HA can thus be recognized as being similar to natural mineralized tissue.

In conclusion, the proposed process of apatite assembly is summarized schematically in Fig. 6. The multi-walled surfaces of the nanotubes provide abundant sites for the nucleation of apatite in the solution. A single unit of the bamboo structure was used as an example to illustrate the mineralization process. The carboxylic groups on the surface act as the coordination bonds for chelation of calcium in HA crystals. The nucleated apatite temporarily attaches along the interface of carbon layers (Fig. 6b). Moreover, the growing apatite crystals can be easily detached from the MWCNTs (Fig. 6c) due to weak functionalization of the binding groups and the unstable support of the growing apatite crystals on the curved surface of the MWCNT. The nHA polycrystal fibrils are assembled into a parallel array of spindle-shaped units. When the apatite assembly unit reaches a sufficient size, it separates from the carbon nanotubes probably due to the pertubation from stirring. This exposes the surface of the MWCNTs for further nucleation (Fig. 6a).

This separated spindle-shaped unit can be used as the building block for assembling high-level biomaterials. An important application is the development of substitute material for hard tissue using this biomimetic method. For example, enamel is a hard, wear-resistant material with highly ordered micro/nano architecture consisting of carbonated HA crystallites assembled into a woven prism structure. Organic matrix components make up less than 2% of the enamel [5,6]. Unlike bone tissues, enamel does not contain collagen and does not undergo remodeling. On the other hand, 60% of the underlying dentine consists

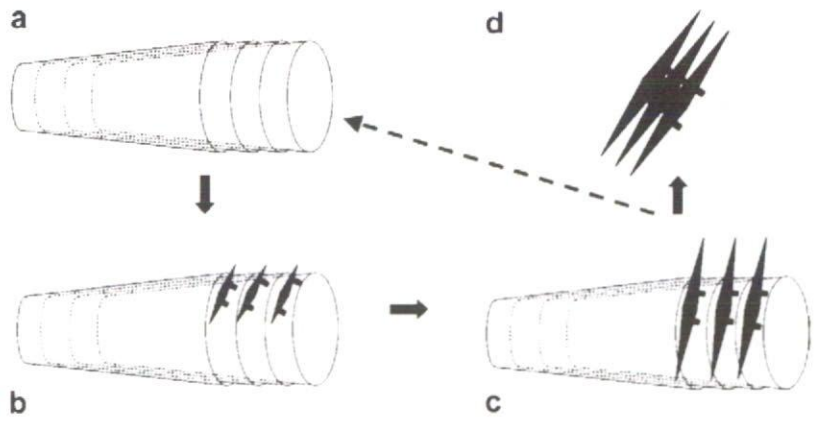

Fig. 6. Schematic illustration of the assembly process of HA on MWCNTs. (a) Bamboo unit of the MWCNTs. (b) The nucleation of HA on the surface of CNTs. (c) The growth of the HA fibrils occurs on the surface of the CNTs. The HA fibrils are oriented parallel to each other and assemble into a spindle unit. (d) The assembled HA dissociates from the MWCNTs, leaving an open site for formation of new HA if sufficient calcium and phosphate ions are present in the solution. Red rods refer to the chemical functional bonds and blue prisms refer to nHA polycrystal fibril. (For interpretation of the references to colour in this figure legend, the reader is referred to the web version of this article.)

of mineral crystals, which grow in the gaps between staggered or overlapped collagen fibrils. Until now, there has been no effective method for the preparation of hierarchical materials such as enamel and dentine. The nanoscale similarity between nHA assembled on MWCNTs and natural enamel tissue opens the possibility of fabricating biomimetic materials similar to natural tooth. In view of previously unsuccessful attempts to mimic the hierarchical structure of enamel on the nanometer and micrometer scales [33], carbon nanotubes may provide a promising platform for further research in the systematic incorporation and assembly of organic, inorganic and biological composites in a template for nucleation, growth and alignment over multiple length scales. Therefore, future work will be focused on the high-level self-assembly of functionalized MWCNTs and HA, which could lead to a more complete imitation of natural hard tissue.

Acknowledgements

This work was supported in part by the JSPS Program in Japan, the 2002–2005 Health and Labor Sciences Research Grants for Research on Advanced Medical Technology: "Tissue Reaction and Biomedical Application of Nanotubes, Nanoparticles and Microparticles (H14-Nano-021)" from the Ministry of Health, Labor, Sports and Welfare, Japan, and NUS LKY PDF fellowship in Singapore.

References

[1] Landis WJ, Song MJ, Leith A. Mineral and organic matrix interaction in normally calcifying tendon visualized in three dimensions by high-voltage electron microscopic tomography and graphic image reconstruction. J Struct Biol 1993;110:39–54.
[2] Lowenstam HA, Weiner S. On biomineralization. New York: Oxford University Press; 1989. p. 35–40.
[3] Zhang S. Fabrication of novel biomaterials through molecular self-assembly. Nat Biotechnol 2003;21:1171–8.
[4] Hartgerink JD, Beniash E, Stupp SI. Self-assembly and mineralization of peptide-amphiphile nanofibers. Science 2001;294:1684–8.
[5] Du C, Falini G, Fermani S, Abbott C, Moradian-Oldak J. Supramolecular assembly of amelogenin nanospheres into birefringent microribbons. Science 2005;307:1450–4 [Erratum: Science 2005; 309:2166].
[6] Moradian-Oldak J, Du C, Falini G. On the formation of amelogenin microribbons. Eur J Oral Sci 2006;114:289–96.
[7] Arthur V. A window on biomineralization. Science 2005;307:1419–20.
[8] Murphy WL, Mooney DJ. Bioinspired growth of crystalline carbonate apatite on biodegradable polymer substrata. J Am Chem Soc 2002;9:1910–7.
[9] Iijima S. Helical microtubules of graphitic carbon. Nature 1991;354:56–8.
[10] Sun YP, Huang W, Lin Y, Fu K, Kitaygorodskiy A, Riddle LA, et al. Soluble dendron-functionalized carbon nanotubes: preparation, characterization, and properties. Chem Mater 2001;13:2864–9.
[11] Jiang K, Eitan A, Schadler LS, Ajayan PM, Siegel RW. Selective attachment of gold nanoparticles to nitrogen-doped carbon nanotubes. Nano Lett 2003;3:275–7.
[12] Djalali R, Chen YF, Matsui H. Au nanocrystal growth on nanotubes controlled by conformations and charges of sequenced peptide templates. J Am Chem Soc 2003;125:5873–9.
[13] Che G, Lakshmi BB, Fisher ER, Martin CR. Carbon nanotubule membranes for electrochemical energy storage and production. Nature 1998;393:346–9.
[14] Han L, Wu W, Kirk Louis F, Luo J, Maye MM, Kariuki NN, et al. A direct route toward assembly of nanoparticle-carbon nanotube composite materials. Langmuir 2004;20:6019–25.
[15] Rosca ID, Watari F, Uo M, Akasaka T. Oxidation of mutiwalled carbon nanotubes by nitric acid. Carbon 2005;43:3124–31.
[16] Li YH, Xu C, Wei B, Zhang X, Zheng M, Ajayan PM. Self-organized ribbons of aligned carbon nanotubes. Chem Mater 2002;14:483–5.
[17] Correa-Duarte MA, Wagner N, Rojas-Chapana J, Morsczeck C, Thie M, Giersig M. Fabrication and biocompatibility of carbon nanotube-based 3D networks as scaffolds for cell seeding and growth. Nano Lett 2004;4:2233–6.
[18] Yu ZH, Brus LE. Reversible oxidation effect in Raman scattering from metallic single-wall carbon nanotubes. J Phys Chem 2000;A104: 10995–9.
[19] Kuznetsova A, Popova I, Yates JT, Bronikowski MJ, Huffman CB, Liu J, et al. Oxygen-containing functional groups on singlewall carbon nanotubes: NEXAFS and vibrational spectroscopic studies. J Am Chem Soc 2001;123:10699–704.
[20] Kukovecz A, Kramberger C, Holzinger M, Kuzmany H, Schalko J, Mannsberger M, et al. On the stacking behavior of functionalized single-wall carbon nanotubes. J Phys Chem 2002;B106:6374–80.
[21] Liao S, Watari F, Uo M, Ohkawa S, Tamura K, Wang W, et al. The preparation and characteristics of a carbonated hydroxyapatite/collagen composite at the room temperature. J Biomed Mater Res 2005;74B:817–21.
[22] MDI JADE6 software, XRD pattern processing. Materials Data, Inc.; 2003.
[23] Klug HP, Alexander LE. X-ray diffraction procedures for polycrystalline and amorphous materials. New York: Wiley Interscience; 1974.
[24] Suchanek WL, Shuk P, Byrappa K, Riman RE, TenHuisen KS, Janas VF. Mechanochemical-hydrothermal synthesis of carbonated apatite powders at room temperature. Biomaterials 2002;23:699–710.
[25] Peters F, Schwarz K, Epple M. The structure of bone studied with synthrotron X-ray diffraction, X-ray absorption spectroscopy and thermal analysis. Thermochim Acta 2000;361:131–8.
[26] Zhang GY, Ma XC, Zhong DY, Wang EG. Polymerized carbon nitride nanobells. J Appl Phys 2002;91:9324–32.
[27] Wang YY, Tang GY, Koeck FAM, Brown B, Garguilo JM, Nemanich RJ. Experimental studies of the formation process and morphologies of carbon nanotubes with bamboo mode structures. Diam Relat Mater 2004;13:1287–91.
[28] Gerard Lavin J, Subramoney S, Ruoff RS, Berber S, Tomanek D. Scrolls and nested tubes in multiwall carbon nanotubes. Carbon 2002;40:1123–30.
[29] Rhee SH, Lee JD, Tanaka J. Nucleation of hydroxyapatite crystal through chemical interaction with collagen. J Am Ceram Soc 2000;83:2890–2.
[30] Akasaka T, Watari F, Sato Y, Tohji K. Apatite formation on carbon nanotubes. Mater Sci Eng C 2006;26:675–8.
[31] Holmes DF, Graham HK, Trotter JA, Kadler KE. STEM/TEM studies of collagen fibril assembly. Micron 2001;32:273–85.
[32] Zhang W, Huang KL, Liao SS, Cui FZ. Nucleation sites of calcium phosphate crystals during collagen mineralization. J Am Ceram Soc 2003;86:1052–4.
[33] Du C, Moradian-Oldak J. Tooth regeneration: challenges and opportunities for biomedical material research. Biomed Mater 2006;1:R10–7.

Available online at www.sciencedirect.com
ScienceDirect
Gene 395 (2007) 108–115
GENE
SECTION
FUNCTIONAL GENOMICS
www.elsevier.com/locate/gene

Direct observation of histone H2B-YFP fusion proteins and transport of their mRNA between conjugating *Paramecia*

Yasuhiro Takenaka [a], Akira Yanagi [b], Hiromi Masuda [a,c], Youji Mitsui [d], Hiroshi Mizuno [a,c], Nobuyuki Haga [b,*]

[a] *Department of Biochemistry, National Institute of Agrobiological Sciences, Tsukuba, Ibaraki 305-8602, Japan*
[b] *Department of Biotechnology, Ishinomaki Senshu University, Ishinomaki, Miyagi 986-8580, Japan*
[c] *VALWAY Technology Center, NEC Soft, Ltd., 1-18-7, Koto-ku, Tokyo 136-8627, Japan*
[d] *Department of Pharmaceutical Technology, Faculty of Pharmaceutical Sciences at Kagawa Campus, Tokushima Bunri University, Kagawa 769-2193, Japan*

Received 1 December 2006; received in revised form 25 January 2007; accepted 6 February 2007
Available online 28 February 2007
Received by T. Sekiya

Abstract

Cytoplasmic exchange between conjugating cells of *Paramecium caudatum* has been implicated by mating experiments using wild-type and behavioral mutant cells. To observe macromolecular transport between mating cells, we cloned and expressed the *P. caudatum* histone H2B gene as a fusion protein attached to an enhanced yellow fluorescent protein (YFP) named PcVenus. Significant fluorescent signals derived from histone H2B–PcVenus were detected throughout the macro- and micronuclei of transformant cells after microinjection of the expression vector. The normal growth and high mating reactivity of the transformants indicated that H2B–PcVenus functioned normally. Seven hours after a transformant cell expressing histone H2B–PcVenus was mated with an untransformed complementary mating-type cell, fluorescence derived from histone H2B–PcVenus was emitted from the macronuclei of the untransformed cell. About 48 h later, the fluorescent signal was detected not only in the macro- and micronuclei of untransformed cells but also in the macronuclear anlagen of both mating cells. This suggests that conjugant cells share parental histones during meiosis and subsequent DNA rearrangement. Single-cell RT-PCR analysis demonstrated the presence of H2B–PcVenus mRNA in untransformed cells 15 and 24 h after conjugation. We concluded that at least the mRNA of histone H2B–PcVenus was transferred from the transformed, to the untransformed cell during conjugation.

Keywords: Conjugation; Histone; Fluorescent protein; *Paramecium*; Transformation

1. Introduction

The ciliated unicellular eukaryotic protozoan, *Paramecium*, has dimorphic nuclei, a somatic macronucleus and a germinal micronucleus, which co-exist within the same cell. The somatic macronucleus is highly polyploid, transcriptionally active, and divides amitotically during vegetative cell division whereas the germinal micronucleus is diploid, transcriptionally inactive, and divides mitotically. During conjugation, that is, sexual process between cells of complementary mating types, the micronucleus undergoes meiosis and mitosis to produce pronuclei that are mutually exchanged between the mating cells. Thereafter, the macronucleus is degraded, and new macronuclei are reorganized from the division products of a synkaryon.

During conjugation, mating cells interact with each other through cilia and form large agglutinates. About 1 h after the formation of mating clumps, the initial stage or holdfast union of mating pairs is formed. The second stage or paroral union occurs about 2 h after mating and then cytoplasmic bridges between mating cells are formed. Intercellular cytoplasmic exchange in

Abbreviations: GFP, green fluorescent protein; RT, reverse transcription; RACE, rapid amplification of cDNA ends; ORF, open reading flame; PAGE, polyacrylamide gel electrophoresis; PBS, phosphate buffered saline; PFA, paraformaldehyde; YFP, yellow fluorescent protein.

* Corresponding author. Tel.: +81 225 22 7716; fax: +81 225 22 7746.
E-mail address: haga@isenshu-u.ac.jp (N. Haga).

0378-1119/$ - see front matter © 2007 Elsevier B.V. All rights reserved.
doi:10.1016/j.gene.2007.02.013

Paramecium caudatum has been studied using a caudatum non-reversal (CNR) behavioral mutant. About 2 h after a paroral union is formed between cnrC mutants and wild-type cells, the mutants undergo a phenotypic change to the wild-type (Hiwatashi et al., 1980). Because the phenotype of cnrC mutants changes even after microinjecting wild-type cytoplasm into cnrC cells, the genetic defect of the cnrC mutant is apparently rescued through the transfer of a cytoplasmic curing factor from the wild-type during conjugation (Hiwatashi et al., 1980; Haga et al., 1983). However, the transport of macromolecules such as protein or RNA has not yet been directly demonstrated using molecular biological means.

We constructed the expression vector, pTub-tel3 (pTT3), that constitutively expresses a target protein in *P. caudatum* (Takenaka et al., 2002). We then created a highly codon-optimized GFP (green fluorescent protein) gene to use as a reporter, and demonstrated the effectiveness of codon-optimization and the usefulness of pTT3. The entire body of cells transformed by the codon-optimized GFP emitted intense GFP fluorescence. When the transformant was conjugated with an untransformed cell, GFP fluorescence was detected in the transformant even after conjugation, whereas no significant fluorescence was evident in the untransformed cell.

Here, we further explored the application of the expression vector to observe a target protein in specific subcellular organelles in a live *Paramecium* cell. We created a superenhanced yellow fluorescent protein, PcVenus, by altering 8 amino acid residues of codon-optimized GFP to improve its intensity. We then expressed an endogenous protein fused to PcVenus to localize it in a specific subcellular organelle, which would enable more sensitive detection than labeling the whole cell body since the concentration of a tagged protein packed in a small specific organelle would be higher. We partnered the *P. caudatum* nuclear protein, histone H2B, with PcVenus. Expressing the histone H2B–PcVenus fusion protein under the control of the α-tubulin promoter resulted in a specifically intense fluorescent signal that was detectable throughout the macro- and micronuclei of the transformant cells. We observed the dynamics of localization of histone H2B–PcVenus during conjugation between transformed and untransformed cells. Single-cell RT-PCR analysis of transformed and untransformed cells localized H2B–PcVenus mRNA in untransformed cells after mating. The results implied that histone H2B–PcVenus mRNA, and probably protein, was transported through cytoplasmic bridges between mating partners. We discuss the biological importance of the mutual exchange of macromolecules in mating pairs and the shared use of histones among old and new generations of nuclei.

2. Materials and methods

2.1. Stocks and cultures of P. caudatum

Histone H2B cDNA was cloned from the trichocyst non-discharge, syngen 3 (O-type) mutant (tnd2/tnd2), KoscA4. The cnr mutant, KNZcA2-11 or 16B001SIIB5, was the mating partner for the histone H2B–PcVenus transformant which is wild-type in terms of swimming behavior. KNZcA2-11 and 16B001SIIB5 cannot swim backwards in a high potassium solution (80 mM KCl, 1 mM $CaCl_2$, 1 mM Tris–HCl, pH 7.2), rendering it easily distinguishable from transformed cells. The culture medium and conditions were as described (Takenaka et al., 2002).

2.2. Cloning of P. caudatum histone H2B gene

We synthesized *P. caudatum* cDNA from 1 μg of total RNA using the SMART RACE cDNA amplification kit (Clontech). Degenerate primers were designed based on the conserved regions of the H2B sequences of *Tetrahymena thermophila* (nos. X05543 and X05544). The 5′ end of *P. caudatum* histone H2B cDNA was amplified using the PcHis H2B LP350 primer, 5′-AACTTGGTGACRGCYTTKGTWCCTTC-3′, and Universal Primer Mix (Clontech). After sequencing the 5′-RACE (rapid amplification of cDNA ends) products and identifying homology with known H2B proteins using the BLAST program, 2 full length H2B cDNAs were amplified using PcHis H2B UP0-1, (5′-CACCATGGCACCATCCAAATCCC-CAGCT-3′) and PcHis H2B UP0-2 (5′-CACCATGGCACCAT-CAAAATCACCAAAA-3′), respectively, with Universal Primer Mix. The complete sequences of the *P. caudatum* histone H2B genes (referred to as PcH2B1 and PcH2B2, respectively) were deposited in the DDBJ/EMBL/GenBank database under accession nos. AB195236 and AB195237. We conducted multiple alignments of amino acid sequences of the histone H2B2 protein of *Paramecium* with other organisms using the program Clustal W (1.8) with the default parameters.

2.3. Site-directed mutagenesis and construction of the histone H2B–PcVenus expression vector

We constructed a *P. caudatum* expression vector and the codon-optimized GFP gene, GFPmut3.3, as described (Takenaka et al., 2002). The novel variant of yellow fluorescent protein, Venus, which quickly folds to the mature form has been reported elsewhere (Nagai et al., 2002). To create a codon-optimized Venus gene for efficient expression in *Paramecium*, we introduced 16 site-specific mutations into the GFPmut3.3 gene, which resulted in 8 amino acid substitutions. The complete nucleotide sequence of PcVenus, a codon-optimized and superenhanced yellow fluorescent protein, has been deposited in the DDBJ database under accession no. AB195239.

2.4. Microinjection and fluorescence microscopy

The pTT3 H2B–PcVenus expression vector was purified using a QIAfilter Plasmid Maxi Kit (Qiagen), digested with *Bam* HI and microinjected into the macronucleus as described (Takenaka et al., 2002). Transformant clones were stained with 5 μM of Hoechst 33342 for 30 min, washed with K-DS (Dryl's solution modified by substituting KH_2PO_4 for NaH_2PO_4, pH 7.0) and suspended in K-DS containing 7 mg/ml bovine serum albumin. The cells were air-dried, mounted using Entellan® New (Merck), and observed under a Nikon OPTIPHOT microscope using a Plan Fluor 20× (N.A. 0.75) objective. The excitation and emission filters for PcVenus observation were EX450-490 and BA520, respectively. The cells were photographed using a Nikon camera

FX-35DX with exposure control by Nikon UFX-II. To analyze histone H2B–PcVenus during conjugation, transformed and untransformed cells were starved for 1–2 days to induce mating activity, and then cells from each culture were mixed and paired. Heterotypic mating pairs were selected according to behavior in the high potassium test solution and isolated into new depression slides about 3 h after complementary mating types were mixed.

2.5. Single-cell RT-PCR analysis

Transformants expressing histone H2B–PcVenus were mated with untransformed 16B001SIIB5 (CNR mutant) cells. Heterotypic pairs were identified in the high potassium solution (see Section 2.1) and isolated into K-DS. At 30 min after mixing, the swimming behavior of mating pairs was tested again after separation by pipetting in the high potassium solution to identify transformed and untransformed cells. The swimming behavior of exconjugant cells, which had normally separated during conjugation, was also tested after 15 and 24 h, and they were individually harvested. Total RNA from cells prepared using the RNeasy Micro kit (Qiagen) according to the manufacturer's instructions, was reverse transcribed using Sensiscript reverse transcriptase (Qiagen). Fragments of PcVenus (351 bp) or α-tubulin (218 bp) were amplified using Advantage 2 polymerase (Clontech) with PcVenus- or α-tubulin-specific primers, respectively (Takenaka et al., 2002).

3. Results

3.1. Cloning the P. caudatum histone H2B gene

The protein and nucleotide sequences of the *Paramecium* histone H2B gene were not found in the GenBank database. Using degenerate primers based on the conserved regions of known histone H2B genes, fragments of *P. caudatum* histone H2B cDNA were amplified from *P. caudatum* using RACE cDNA. The nucleotide and deduced amino acid sequences of *P. caudatum* histone H2B were then deposited in the DDBJ/EMBL/GenBank database (see Section 2.2). We identified several candidates of histone H2B by a BLAT search (http://www.genoscope.cns.fr/blat-server/cgi-bin/paramecie/webBlat) of the *Paramecium tetraurelia* macronuclear genome database (Aury et al., 2006) using amino acid sequence of *P. caudatum* histone H2B as a query. The top-ranked candidate of histone H2B in *P. tetraurelia* genome was found on scaffold_4 and showed high identity (98.4%) to *P. caudatum* H2B (Fig. 1). The expression of GFP-histone H2B fusion protein in human cultured cells allows sensitive analysis of chromosome dynamics (Kanda et al., 1998; Kimura and Cook, 2001). Although the degree of homology between human and *P. caudatum* histone H2B is not high (61%), both proteins might share similar functional and structural properties in terms of chromatin formation. Therefore, we selected the H2B gene as the fusion protein.

3.2. Expression of H2B–PcVenus protein in P. caudatum

We created the codon-optimized and superenhanced yellow fluorescent protein, PcVenus, to improve the fluorescence intensity of GFP. The *P. caudatum* histone H2B gene was fused with the PcVenus coding sequence to produce an H2B–PcVenus fusion protein. A fragment of the fusion gene and an expression cassette were cloned into pTT3 (previously referred to as pTub-tel3 expression vector), and named pTT3 H2B–PcVenus (Fig. 2A). The vector was digested with *Bam* HI to expose telomeric repeats at both ends. In addition to a 350-bp subtelomeric region that originated from the *Tetrahymena*

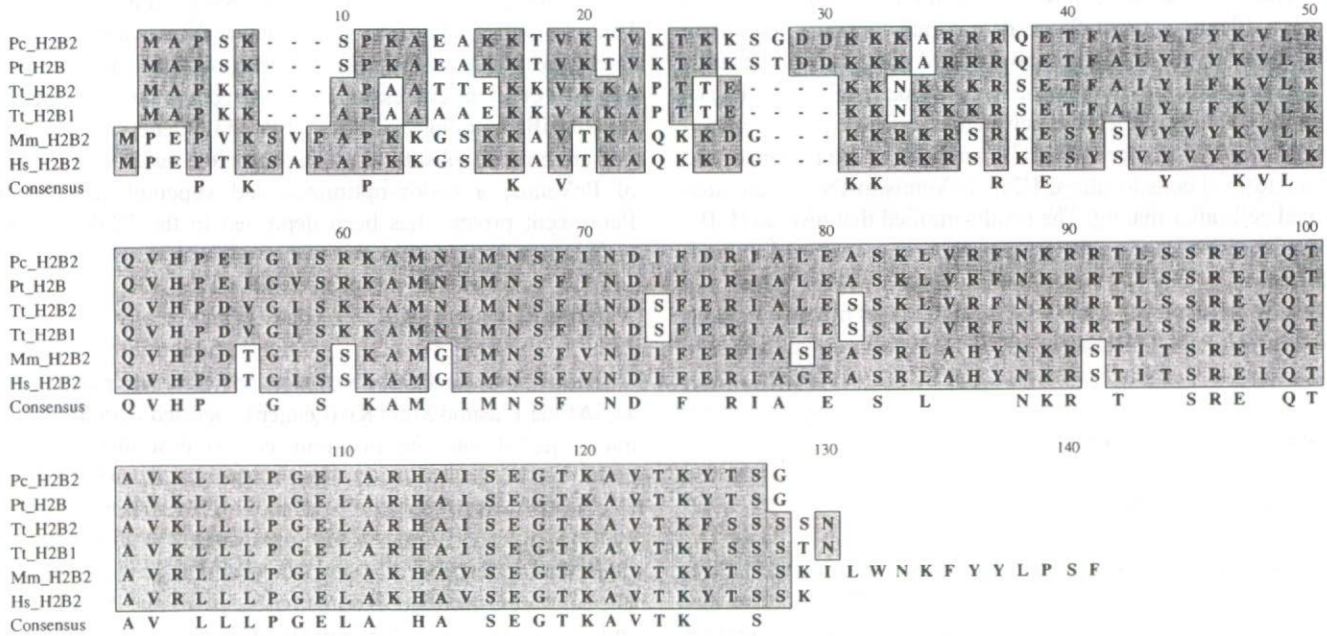

Fig. 1. Multiple alignment of amino acid sequences among six histone H2Bs. Residues are shaded and outlined if at least 67% were identical or similar. Organisms are *Paramecium caudatum* (Pc_H2B2, AB195237), *P. tetraurelia* (Pt_H2B, scaffold_4:11388...12003), *Tetrahymena thermophila* (Tt_H2B1 and Tt_H2B2, X05543 and X05544), *Mus musculus* (Mm_H2B, AAH61044) and *Homo sapiens* (Hs_H2B, AAN06687).